

ALMA [CI]³P₁ –³ P₀ observations of NGC 6240: a puzzling molecular outflow, and the role of outflows in the global α_{CO} factor of (U)LIRGs

CLAUDIA CICONE,^{1,*} PAOLA SEVERGNINI,¹ PADELIS P. PAPADOPOULOS,^{2,3,4} ROBERTO MAIOLINO,^{5,6} CHIARA FERUGLIO,⁷
EZEQUIEL TREISTER,⁸ GEORGE C. PRIVON,⁹ ZHI-YU ZHANG,^{10,11} ROBERTO DELLA CECA,¹ FABRIZIO FIORE,¹²
KEVIN SCHAWINSKI,¹³ AND JEFF WAGG¹⁴

¹INAF - Osservatorio Astronomico di Brera, Via Brera 28, 20121 Milano, Italy

²Department of Physics, Section of Astrophysics, Astronomy and Mechanics, Aristotle University of Thessaloniki, Thessaloniki, Macedonia, 54124, Greece

³Research Center for Astronomy, Academy of Athens, Soranou Efessiou 4, GR-115 27 Athens, Greece

⁴School of Physics and Astronomy, Cardiff University, Queen's Buildings, The Parade, Cardiff, CF24 3AA, UK

⁵Cavendish Laboratory, University of Cambridge, 19 J. J. Thomson Ave., Cambridge CB3 0HE, UK

⁶Kavli Institute of Cosmology Cambridge, Madingley Road, Cambridge CB3 0HA, UK

⁷INAF - Osservatorio Astronomico di Trieste, via G.B. Tiepolo 11, 34143 Trieste, Italy

⁸Instituto de Astrofísica, Facultad de Física, Pontificia Universidad Católica de Chile, Casilla 306, Santiago 22, Chile

⁹Department of Astronomy, University of Florida, 211 Bryant Space Sciences Center, Gainesville, 32611 FL, USA

¹⁰European Southern Observatory, Karl-Schwarzschild-Strae 2, 85748 Garching, Germany

¹¹Institute for Astronomy, University of Edinburgh, Royal Observatory, Blackford Hill, Edinburgh EH9 3HJ, UK

¹²INAF - Osservatorio Astronomico di Roma, via Frascati 33, 00078 Monteporzio Catone, Italy

¹³Institute for Particle Physics and Astrophysics, ETH Zurich, Wolfgang-Pauli-Str. 27, CH-8093 Zurich, Switzerland

¹⁴SKA Organisation, Lower Withington Macclesfield, Cheshire SK11 9DL, UK

(Received June 29, 2018; Revised June 29, 2018; Accepted July 11, 2018)

Submitted to ApJ

ABSTRACT

We present Atacama large millimeter/ submillimeter array (ALMA) and compact array (ACA) [CI]³P₁ –³ P₀ ([CI](1-0)) observations of NGC 6240, which we combine with ALMA CO(2-1) and IRAM Plateau de Bure Interferometer CO(1-0) data to study the physical properties of the massive molecular (H₂) outflow. We discover that the receding and approaching sides of the H₂ outflow, aligned east-west, exceed 10 kpc in their total extent. High resolution (0.24'') [CI](1-0) line images surprisingly reveal that the outflow emission peaks *between* the two active galactic nuclei (AGN), rather than on either of the two, and that it dominates the velocity field in this nuclear region. We combine the [CI](1-0) and CO(1-0) data to constrain the CO-to-H₂ conversion factor (α_{CO}) in the outflow, which is on average 2.1 ± 1.2 M_⊙(K km s⁻¹ pc²)⁻¹. We estimate that 60 ± 20 % of the total H₂ gas reservoir of NGC 6240 is entrained in the outflow, for a resulting mass-loss rate of $\dot{M}_{out} = 2500 \pm 1200 M_{\odot} yr^{-1} \equiv 50 \pm 30$ SFR. This energetics rules out a solely star formation-driven wind, but the puzzling morphology challenges a classic radiative-mode AGN feedback scenario. For the quiescent gas we compute $\langle \alpha_{CO} \rangle = 3.2 \pm 1.8 M_{\odot}(K km s^{-1} pc^2)^{-1}$, which is at least twice the value commonly employed for (ultra) luminous infrared galaxies ((U)LIRGs). We observe a tentative trend of increasing $r_{21} \equiv L'_{CO(2-1)}/L'_{CO(1-0)}$ ratios with velocity dispersion and measure $r_{21} > 1$ in the outflow, whereas $r_{21} \simeq 1$ in the quiescent gas. We propose that molecular outflows are the location of the warmer, strongly unbound phase that partially reduces the opacity of the CO lines in (U)LIRGs, hence driving down their global α_{CO} and increasing their r₂₁ values.

Keywords: galaxies: active — galaxies: evolution — galaxies: individual (NGC 6240) — galaxies: ISM — submillimeter: ISM

1. INTRODUCTION

Massive ($M_{mol} > 10^8 M_{\odot}$) and extended ($r \gtrsim 1$ kpc) outflows of cold and dense molecular (H_2) gas have been discovered in a large number of starbursts and active galactic nuclei (AGNs) (Turner 1985; Nakai et al. 1987; Sakamoto et al. 2006; Fischer et al. 2010; Feruglio et al. 2010; Sturm et al. 2011; Alatalo et al. 2011; Dasyra & Combes 2012; Veilleux et al. 2013; Spoon et al. 2013; Combes et al. 2013; Morganti et al. 2013; Feruglio et al. 2013b; Cicone et al. 2014; García-Burillo et al. 2014, 2015; Zschaechner et al. 2016; Feruglio et al. 2017; Carniani et al. 2017; Barcos-Muñoz et al. 2018; Gowardhan et al. 2018; Fluetsch et al. 2018). Although so far limited mostly to local (ultra) luminous infrared galaxies ((U)LIRGs), these observations indicate that the mass-loss rates of H_2 gas are higher compared to the ionised gas phase participating in the outflows (Carniani et al. 2015; Fiore et al. 2017). Therefore, molecular outflows, by displacing and perhaps removing the fuel available for star formation, can have a strong impact on galaxy evolution. More luminous AGNs host more powerful H_2 winds, suggesting a direct link between the two (Cicone et al. 2014).

The presence of massive amounts of cold and dense H_2 gas outflowing at $v \gtrsim 1000$ km s⁻¹ across kpc scales in galaxies is itself puzzling. A significant theoretical effort has gone into reproducing the properties of multi-phase outflows in the context of AGN feedback models (Cicone et al. 2018). In one of the AGN radiative-mode scenarios, the outflows result from the interaction of fast highly ionised winds launched from the pc-scales with the kpc-scale interstellar medium (ISM), which occurs through a ‘blast-wave’ mechanism (Silk & Rees 1998; King 2010; Zubovas & King 2012; Faucher-Giguère & Quataert 2012; Costa et al. 2014; Gaspari & Sądowski 2017; Biernacki & Teyssier 2018). In this picture, because molecular clouds overtaken by a hot and fast wind are quickly shredded (Brüggen & Scannapieco 2016), it is more likely that the high-velocity H_2 gas forms directly within the outflow, by cooling out of the warmer gas (Zubovas & King 2014; Costa et al. 2015; Nims et al. 2015; Thompson et al. 2016; Richings & Faucher-Giguère 2018). An alternative scenario, not requiring shockwaves, is the direct acceleration of the molecular ISM by radiation pressure on dust (Thompson et al.

2015; Ishibashi & Fabian 2015; Costa et al. 2018). This mechanism is most efficient in AGNs deeply embedded in a highly IR optically thick medium, such as local (U)LIRGs.

In order to advance our theoretical understanding of galactic-scale molecular outflows, we need to place more accurate constraints on their energetics. Indeed, most current H_2 outflow mass estimates are based on a single molecular gas tracer (CO or OH), implying uncertainties of up to one order of magnitude (Veilleux et al. 2017; Cicone et al. 2018). The luminosity of the CO(1-0) line, which is optically thick in typical conditions of molecular clouds, can be converted into H_2 mass through an CO(1-0)-to- H_2 conversion factor (α_{CO}) calibrated using known sources and dependent on the physical state of the gas. For the molecular ISM of isolated (or only slightly perturbed) disk galaxies like the Milky Way, the conventional α_{CO} is $4.3 M_{\odot}(\text{K km s}^{-1} \text{pc}^2)^{-1}$ (Bolatto et al. 2013). Instead, for merger-driven starbursts like most (U)LIRGs, which are characterised by a more turbulent and excited ISM, a lower α_{CO} of $\sim 0.6 - 1.0 M_{\odot}(\text{K km s}^{-1} \text{pc}^2)^{-1}$ is often adopted (Downes & Solomon 1998; Yao et al. 2003; Israel et al. 2015). Such low α_{CO} values have been ascribed to the existence, in the inner regions of these mergers, of a warm and turbulent ‘envelope’ phase of H_2 gas, not contained in self-gravitating clouds (Aalto et al. 1995). However, some recent analyses of the CO spectral line energy distributions (SLEDs) including high- J ($\gtrsim 3$) transitions suggest that near-Galactic α_{CO} values are also possible for (U)LIRGs, especially when a significant H_2 gas fraction is in dense, gravitationally-bound states (Papadopoulos et al. 2012a). Dust-based ISM mass measurements also deliver galactic-type α_{CO} factors for (U)LIRGs, although they depend on the underlying assumptions used to calibrate the conversion (Scoville et al. 2016).

Molecular outflows can be significantly fainter than the quiescent ISM, and so multi-transition observations aimed at estimating their α_{CO} are particularly challenging. Dasyra et al. (2016) and more recently Oosterloo et al. (2017), for the radio-jet driven outflow in IC 5063, derived a low optically-thin α_{CO} of $\sim 0.3 M_{\odot}(\text{K km s}^{-1} \text{pc}^2)^{-1}$, in line with theoretical predictions by Richings & Faucher-Giguère (2018). On the other hand, for the starburst-

* Marie Skłodowska-Curie fellow

driven M82 outflow, Leroy et al. (2015) calculated¹ $\alpha_{\text{CO}}^{2-1} = 1 - 2.5 \text{ M}_{\odot} (\text{K km s}^{-1} \text{ pc}^2)^{-1}$. The detection of high density gas in the starburst-driven outflow of NGC 253 would also favour an α_{CO} higher than the optically thin value (Walter et al. 2017), and a similar conclusion may be reached for the outflow in Mrk 231, found to entrain a substantial amount of dense H₂ gas (Aalto et al. 2012, 2015; Cicone et al. 2012; Lindberg et al. 2016).

An alternative method for measuring the molecular gas mass, independent of the α_{CO} factor, is through a tracer such as the ³P₁ –³P₀ transition of neutral atomic carbon (hereafter [CI](1-0)). This line, optically thin in most cases, has an easier partition function than molecules and excitation requirements similar to CO(1-0)². More importantly [CI] is expected to be fully coexisting with H₂ (Papadopoulos et al. 2004; Papadopoulos & Greve 2004). Therefore, by combining the information from CO(1-0) and [CI](1-0) it is possible to derive an estimate of the α_{CO} value. Similar to any optically thin species used to trace H₂ (e.g. dust, ¹³CO), converting the [CI](1-0) line flux into a mass measurement is plagued by the unavoidable uncertainty on its abundance. However, in this regard, recent calculations found not only that the *average* [C/H₂] abundance in molecular clouds is more robust than that of molecules such as CO, but also that [CI] can even trace the H₂ gas where CO has been severely depleted by cosmic rays (CRs, Bisbas et al. 2015, 2017).

In this work we use new Atacama large millimeter/ submillimeter array (ALMA) and Atacama compact array (ACA) observations of the [CI](1-0) line in NGC 6240 to constrain the physical properties of its molecular outflow. NGC 6240 is a merging LIRG hosting two AGNs with quasar-like luminosities (Puccetti et al. 2016). The presence of a molecular outflow was suggested by van der Werf et al. (1993) based on the detection of high-velocity wings of the ro-vibrational H₂ $v = 1 - 0$ S(1) 2.12 μm line and by Iono et al. (2007) based on the CO(3-2) kinematics, and it was later confirmed by Feruglio et al. (2013b) using IRAM PdBI CO(1-0) observations. This is one of the first interferometric [CI](1-0) observations of a local galaxy (see also Krips et al. 2016), and - to our knowledge - the first spatially-resolved [CI](1-0) observation of a molecular

outflow in a quasar. Probing the capability of [CI](1-0) to image molecular outflows is crucial: besides being an alternative H₂ tracer independent of the α_{CO} factor, [CI](1-0) is also sensitive to CO-poor gas, which may be an important component of molecular outflows exposed to strong far-ultraviolet (UV) fields (Wolfire et al. 2010) or CR fluxes (Bisbas et al. 2015, 2017; Krips et al. 2016; González-Alfonso et al. 2018). Moreover, testing [CI](1-0) as a sensitive molecular probe in a local and well-studied galaxy such as NGC 6240 has a great legacy value for studies at $z > 2$, where the [CI] lines are very valuable tracers of the bulk of the molecular gas accessible with ALMA (Zhang et al. 2016).

The paper is organised as follows: in § 2 we describe the data; in § 3.1 we present the CO(1-0), CO(2-1), and [CI](1-0) outflow maps and the [CI](1-0) line moment maps. In § 3.2-§ 3.3 we identify the outflowing components of the molecular line emission and derive the α_{CO} and r_{21} values separately for the quiescent ISM and the outflow. The outflow energetics is constrained in § 3.4. In § 3.5 we study the variations of α_{CO} and r_{21} as a function of σ_v and distance of the different spectral components from the nucleus. Our findings are discussed in § 4 and summarised in § 5. Throughout the paper we adopt a standard Λ CDM cosmological model with $H_0 = 67.8 \text{ km s}^{-1} \text{ Mpc}^{-1}$, $\Omega_{\Lambda} = 0.692$, $\Omega_{\text{M}} = 0.308$ (Planck Collaboration et al. 2016). At the distance of NGC 6240 (redshift $z = 0.02448$, luminosity distance $D_L = 110.3 \text{ Mpc}$), the physical scale is $0.509 \text{ kpc arcsec}^{-1}$. Uncertainties correspond to 1σ statistical errors. The units of $\alpha_{\text{CO}} [\text{M}_{\odot} (\text{K km s}^{-1} \text{ pc}^2)^{-1}]$ are sometimes omitted.

2. OBSERVATIONS

The Band 8 observations of the [CI](1-0) ($\nu_{\text{rest}}^{[\text{CI}]} = 492.16065 \text{ GHz}$) emission line in NGC 6240 were carried out in May 2016 with the 12 m-diameter antennas of ALMA and in August 2016 with the 7 m-diameter antennas of the Atacama Compact Array (ACA) as part of our Cycle 3 programme 2015.1.00717.S (PI: Cicone). The ALMA observations were effectuated in a compact configuration with 40 antennas (minimum and maximum baselines, $b_{\text{min}} = 15 \text{ m}$, $b_{\text{max}} = 640 \text{ m}$), yielding an angular resolution (AR) of $0.24''$ and a maximum recoverable scale (MRS) of $2.48''$. Only one of the two planned 0.7 h-long scheduling blocks was executed, and the total on-source time was 0.12 h. The PWV was 0.65 mm and the average system temperature was $T_{\text{sys}} = 612 \text{ K}$. The ACA observations were performed using nine antennas with $b_{\text{min}} = 9 \text{ m}$ and $b_{\text{max}} = 45 \text{ m}$, resulting in AR= $2.4''$ and MRS= $14''$. The total ACA observing time was 3.5 h, of which 0.7 h on source. The average

¹ By using the CO(2-1) transition

² CO(1-0) and [CI](1-0) are similar in critical density but $E_{10}/k_b=5.5 \text{ K}$ for CO and 23 K for [CI]; however, as long as most of the H₂ gas has $T_k > 15 - 20 \text{ K}$, as expected, the E/k_b difference between the two lines makes no real excitation difference in the level population (Papadopoulos et al. 2004).

PWV and T_{sys} were 0.7 mm and 550 K, respectively. J1751+0939 and Titan were used for flux calibration, J1924-2914 for bandpass calibration, J1658+0741 and J1651+0129 for phase calibration.

We employed the same spectral setup for the ALMA and the ACA observations. Based on previous CO(1-0) observations of NGC 6240 (Feruglio et al. 2013b,a), and on the knowledge of the concurrence of the [CI](1-0) and CO(1-0) emissions, we expected the [CI](1-0) line to be significantly broad (full width at zero intensity, $FWZI > 1000 \text{ km s}^{-1}$). Therefore, to recover both the broad [CI](1-0) line and its adjacent continuum, we placed two spectral windows at a distance of 1.8 GHz, overlapping by 75 MHz in their central 1.875 GHz-wide full sensitivity part, yielding a total bandwidth of 3.675 GHz (2293 km s^{-1}) centred at $\nu_{obs}^{[CI]} = 480.40045 \text{ GHz}$.

After calibrating separately the ALMA and ACA datasets with the respective scripts delivered to the PI, we fit and subtracted the continuum in the uv plane. This was done through the CASA³ task `uvcontsub`, by using a zeroth-order polynomial for the fit, and by estimating the continuum emission in the following line-free frequency ranges: $478.568 < \nu_{obs}[\text{GHz}] < 478.988$ and $481.517 < \nu_{obs}[\text{GHz}] < 482.230$. The line visibilities were then deconvolved using `clean` with Briggs weighting and robust parameter equal to 0.5. A spectral binning of $\Delta\nu = 9.77 \text{ MHz}$ (6 km s^{-1}) was applied, and the cleaning masks were chosen interactively. In order to improve the image reconstruction, following the strategy adopted by Hacar et al. (2018), we used the cleaned ACA data cube corrected for primary beam as a source model to initialise the deconvolution of the ALMA line visibilities (parameter ‘`modelimage`’ in `clean`). The synthesised beams of the resulting ACA and ALMA image data cubes are $4.55'' \times 2.98''$ (PA = -53.57 deg) and $0.29'' \times 0.24''$ (PA = 113.18 deg), respectively. In addition, a lower resolution ALMA [CI](1-0) line data cube was produced by applying a tapering (outer taper of $1.4''$), which resulted in a synthesised beam of $1.28'' \times 1.02''$ (PA = 77.49 deg). Primary beam correction was applied to all datasets. We checked the accuracy of the ALMA and ACA relative flux scales by comparing the flux on the overlapping spatial scales between the two arrays, and found that they are consistent within the Band 8 calibration uncertainty of 15%.

As a last step, in order to maximise the uv coverage and the sensitivity to any extended structure possibly

filtered out by the ALMA data, we combined the (tapered and non) ALMA image data cubes with the ACA one using the task `feather`. For a detailed explanation of `feather` we refer the reader to the CASA cookbook⁴. The same steps were used to produce all the interferometric maps shown in this paper, i.e.: (i) `clean` of ACA visibilities followed by primary beam correction, (ii) `clean` of ALMA visibilities by using the ACA images as a source model followed by primary beam correction, and (iii) `feather` of the ACA and ALMA images. The resulting ACA+ALMA merged images inherit the synthesised beam and cell size (the latter set equal to $0.01''$ and $0.2''$ respectively for the higher and lower resolution data) of the corresponding input ALMA images. At the phase tracking centre (central beam), the 1σ sensitivities to line detection, calculated using the line-free spectral channels, are $1.4 \text{ mJy beam}^{-1}$ and 5 mJy beam^{-1} per $dv = 50 \text{ km s}^{-1}$ spectral channel, respectively for the higher and lower resolution [CI](1-0) line data cubes. The sensitivity decreases slightly with distance from the phase center. At a radius of $5''$, the [CI](1-0) line sensitivities per $dv = 50 \text{ km s}^{-1}$ spectral channel are $3.3 \text{ mJy beam}^{-1}$ and $5.5 \text{ mJy beam}^{-1}$.

In this paper we make use of the IRAM PdBI CO(1-0) data previously presented by Feruglio et al. (2013b,a). The CO(1-0) line image data cube used in this analysis has a synthesised beam of $1.42'' \times 1.00''$ (PA = 56.89 deg) and a cell size of $0.2''$. The CO(1-0) 1σ line sensitivity per $dv = 50 \text{ km s}^{-1}$ spectral channel is $0.6 \text{ mJy beam}^{-1}$ at the phase center, and $0.65 \text{ mJy beam}^{-1}$ at a $5''$ radius.

Our analysis also includes ALMA Band 6 (programme 2015.1.00370.S, PI: Treister) snapshot (one minute on source) observations of NGC 6240 targeting the CO(2-1) transition, which were performed in January 2016 (PWV = 1.2 mm) using the compact configuration (AR = $1.2''$, MRS = $10''$). These observations were executed in support of the long baseline campaign carried out by Treister et al. (in prep). We calibrated the data using the script for PI, estimated the continuum from the line-free spectral ranges ($224.106 < \nu_{obs}[\text{GHz}] < 224.279$ and $225.780 < \nu_{obs}[\text{GHz}] < 225.971$) and subtracted it in the uv plane. We deconvolved the line visibilities using `clean` with Briggs weighting (robust = 0.5) and applied a correction for primary beam. The final CO(2-1) cleaned data cube has a synthesised beam of $1.54'' \times 0.92''$ (PA = 60.59 deg) and a cell size of $0.2''$. The 1σ CO(2-1) line sensitivity per $dv = 50 \text{ km s}^{-1}$ channel is $0.80 \text{ mJy beam}^{-1}$ at the phase centre and 1 mJy beam^{-1} at a $5''$ radius.

³ Common Astronomy Software Applications (McMullin et al. 2007).

⁴ Available at <https://casa.nrao.edu>

In the analysis that follows, the comparison between the CO(1-0), CO(2-1), and [CI](1-0) line tracers in the molecular outflow of NGC 6240 will be done by using the lower resolution ALMA+ACA [CI](1-0) data cube, which matches in angular resolution ($\sim 1.2''$) the IRAM PdBI CO(1-0) and ALMA CO(2-1) data. Unless specified, quoted errors include the systematic uncertainties on the measured fluxes due to flux calibration, which are 10% for the IRAM PdBI CO(1-0) and ALMA CO(2-1) data, and 15% for the ALMA [CI](1-0) line observations. We report the presence of some negative artefacts, especially in the cleaned CO(1-0) and CO(2-1) datacubes. These are due to the interferometric nature of the observations, which does not allow to properly recover all the faint extended emission in a source with a very bright central peak emission such as NGC 6240. However, the negative features lie mostly outside the region probed by our analysis and they are not expected to significantly affect our flux recovery, since the total CO(1-0) and CO(2-1) line fluxes are consistent with previous single-dish measurements (Costagliola et al. 2011; Papadopoulos et al. 2012b). Our total [CI](1-0) line flux is higher than that recovered by Papadopoulos & Greve (2004) by using the James Clerk Maxwell telescope (JCMT, $\text{FWHM}_{\text{beam}} = 10''$), but lower by $34 \pm 15\%$ than the flux measured by the *Herschel* space observatory (Papadopoulos et al. 2014). This indicates that some faint extended emission has been resolved out and/or that there is additional [CI](1-0) line emission outside the field of view of our observations.

3. DATA ANALYSIS AND RESULTS

3.1. Morphology of the extended molecular outflow and its launch region

With the aim of investigating the extent and morphology of the outflow, we produced interferometric maps of the CO(1-0), CO(2-1), and [CI](1-0) high-velocity emissions. The maps, shown in Fig. 1(a,b,c), were generated by merging together and imaging the uv visibilities corresponding to the blue- and red-shifted wings of the molecular lines, integrated respectively within $v \in (-650, -200)$ km s⁻¹ and $v \in (250, 800)$ km s⁻¹. These are the velocity ranges that, following from the identification of the outflow components performed in § 3.3 (and further discussed in § 4.1 and Appendix B), are completely dominated by the emission from outflowing gas. The data displayed in panels (a,b,c) have a matched spatial resolution equal to $\sim 1.2''$ (details in § 2). Panels (d,e) of Fig. 1 show the maps of the blue and red [CI](1-0) line wings at the native spatial resolution of the ALMA Band 8 observations ($0.24''$, § 2).

The extended (> 5 kpc) components of the outflow are best seen in Fig. 1(a,b,c), whereas panels (d,e) provide a zoomed view of the molecular wind in the inner 1-2 kpc. The bulk of the outflow extends eastward of the two AGNs, as already pointed out in the previous analysis of the CO(1-0) data done by Feruglio et al. (2013b). In addition, we identify for the first time a western extension of the molecular outflow, roughly aligned along the same east-west axis as the eastern component. At the sensitivity allowed by our data, we detect at a S/N > 5 CO emission features associated with the outflow up to a maximum distance of $13.3''$ (6.8 kpc) and $7.2''$ (3.7 kpc) from the nucleus, respectively in the east and west directions (Fig 1a,b,c). The [CI](1-0) map in Fig 1(c) shows extended structures similar to CO, although the limited field of view of the Band 8 observations does not allow us to probe emission beyond a radius of $\sim 7.5''$.

Feruglio et al. (2013b) hinted at the possibility that the redshifted CO detected in NGC 6240 could be involved in the feedback process, but did not explicitly ascribe it to the outflow because of the smaller spatial extent of the red wing with respect to the blue wing. In Figure 2 we directly compare the blue and red line wings using the ALMA CO(2-1) data. Based on their close spatial correspondence, whereby the red wing overlaps with the blue one across more than 7 kpc along the east-west direction, we conclude that both the red-shifted and blue-shifted velocity components trace the same massive molecular outflow. It follows that the eastern and western sides of the outflow are detected in both their approaching and receding components. At east, the blue-shifted emission is brighter than the red-shifted one and dominant beyond a 3.5 kpc radius.

The ALMA [CI](1-0) data can be used to identify with high precision the location of the inner portion of the molecular outflow. Figures 1(d,e) clearly show that the red wing peaks in the midpoint between the two AGNs, and that the blue wing has a maximum of intensity closer to the southern AGN, as already noted by Feruglio et al. (2013b). However, these data reveal for the first time that *neither the blue nor the red-shifted high velocity [CI](1-0) emissions peak exactly at the AGN positions*. The blue wing has a maximum of intensity at $\text{RA}(\text{J2000}) = 16:52:58.8946 \pm 0.0011\text{s}$, $\text{Dec}(\text{J2000}) = +02.24.03.52 \pm 0.02''$, offset by $0.18'' \pm 0.02''$ to the north-east with respect to the southern AGN. The red wing instead peaks at $\text{RA}(\text{J2000}) = 16 : 52 : 58.9224 \pm 0.0007\text{s}$, $\text{Dec}(\text{J2000}) = +02.24.04.0158 \pm 0.007''$, i.e. at an approximately equal distance of $0.8''$ from the two AGNs. The [CI](1-0) red and blue wing peaks are separated by $0.65'' \pm 0.02''$. This separation is consistent with the distance between the CO(2-1) peaks reported

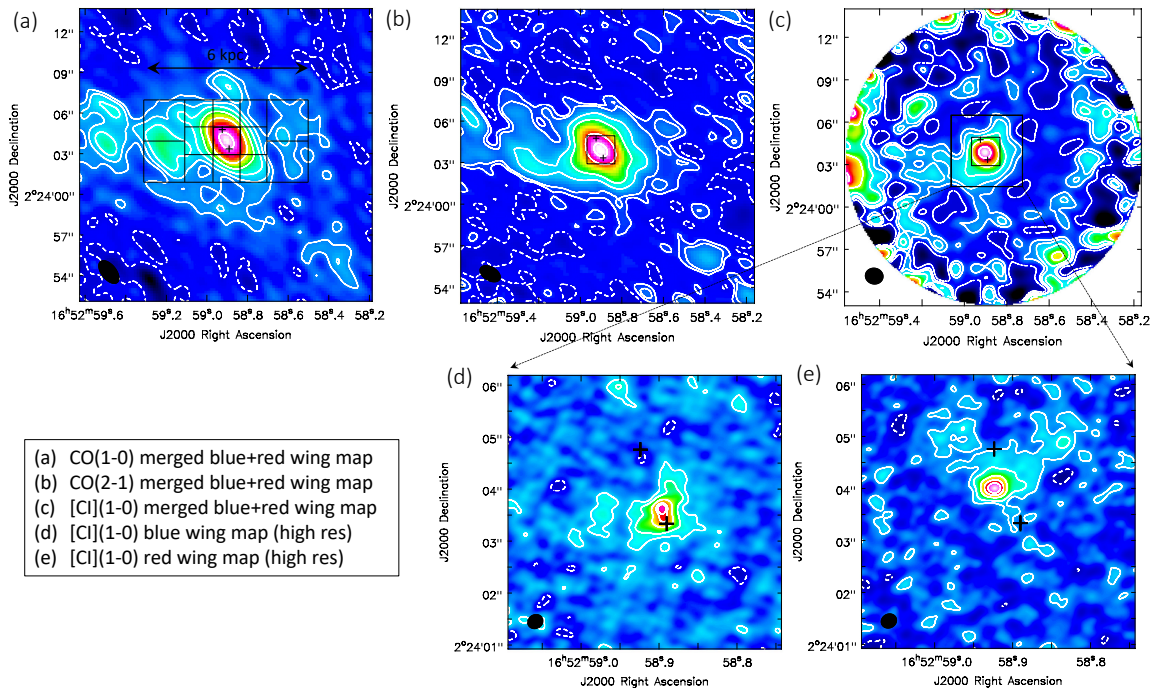


Figure 1. The extended NGC 6240 outflow observed using different molecular gas tracers. The outflow emission, integrated within $v \in (-650, -200)$ km s $^{-1}$ (blue wing) and $v \in (250, 800)$ km s $^{-1}$ (red wing) and combined together, is shown in the maps (a), (b), and (c) respectively for the CO(1-0), CO(2-1), and [CI](1-0) transitions. The three maps have matched spatial resolution ($\sim 1.2''$, details in § 2). Contours correspond to: $(-3\sigma, 3\sigma, 6\sigma, 12\sigma, 24\sigma, 48\sigma, 150\sigma)$ with $1\sigma = 0.14$ mJy beam $^{-1}$ in panel (a); $(-3\sigma, 3\sigma, 6\sigma, 24\sigma, 48\sigma, 200\sigma, 400\sigma)$ with $1\sigma = 0.23$ mJy beam $^{-1}$ in panel (b); $(-3\sigma, 3\sigma, 6\sigma, 12\sigma, 24\sigma, 48\sigma)$ with $1\sigma = 1.23$ mJy beam $^{-1}$ in panel (c). Panels (d) and (e) show the maps of the [CI](1-0) blue and red wings at the original spatial resolution of the ALMA Band 8 data ($0.24''$, details in § 2). Contours correspond to $(-3\sigma, 3\sigma, 6\sigma, 12\sigma, 18\sigma, 20\sigma)$ with $1\sigma = 1.1$ mJy beam $^{-1}$ in panel (d) and $1\sigma = 1$ mJy beam $^{-1}$ in panel (e). The black crosses indicate the VLBI positions of the AGNs from Hagiwara et al. (2011). The synthesised beams are shown at the bottom-left of each map. The grid encompassing the central $12'' \times 6''$ region and employed in the spectral analyses presented in § 3.2 and § 3.3 is drawn in panel (a).

by Tacconi et al. (1999), although in that work they were interpreted as the signature of a rotating molecular gas disk.

The presence of such nuclear rotating H $_2$ structure has been largely debated in the literature, especially due to the very high CO velocity dispersion in this region ($\sigma > 300$ km s $^{-1}$), and to the mismatch between the dynamics of H $_2$ gas and stars (Gerssen et al. 2004; Engel et al. 2010). Following Tacconi et al. (1999) and Bryant & Scoville (1999), if a rotating disk is present, its signature should appear at *lower* projected velocities than those imaged in Fig 1(d,e). In Figure 3 we show the high resolution intensity-weighted moment maps of the [CI](1-0) line emission within $-200 < v[\text{km s}^{-1}] < 250$. The velocity field does not exhibit the characteristic butterfly pattern of a rotating disk, but it presents a highly asymmetric gradient whereby blue-shifted velocities dominate the southern emission, whereas near-systemic and redshifted velocities characterise the northern emission. These features in the velocity field are correlated in both velocity and position with the high velocity wings (Figure 1(d,e)). Furthermore, the right panel

of Fig. 3 shows that the velocity dispersion is uniform ($50 \lesssim \sigma_v[\text{km s}^{-1}] \lesssim 80$) throughout the entire source and enhanced ($\sigma_v \geq 100$ km s $^{-1}$) in a central hourglass-shaped structure extending east-west, which is the same direction of expansion of the larger-scale outflow. This structure has a high- σ_v peak with $\sigma_v \geq 150$ km s $^{-1}$ to the east and another possible peak to the west with $\sigma_v \geq 130$ km s $^{-1}$. Such high- σ_v points coincide with the blue and red-shifted velocity peaks detected in the moment 1 map. Therefore, based on Fig. 3, we conclude that *the molecular gas emission between the two AGNs is dominated by a nuclear outflow expanding east-west and connected to the larger-scale outflow shown in Fig.1*. The regions of enhanced turbulence may represent the places where the outflow opening angle widens up - hence increasing the line-of-sight velocity dispersion and velocity of the molecular gas.

3.2. The α_{CO} values estimated from the integrated spectra: a reference for unresolved studies

Figure 4 shows the CO(1-0), CO(2-1), and [CI](1-0) spectra extracted from the $12'' \times 6''$ -size rectangu-

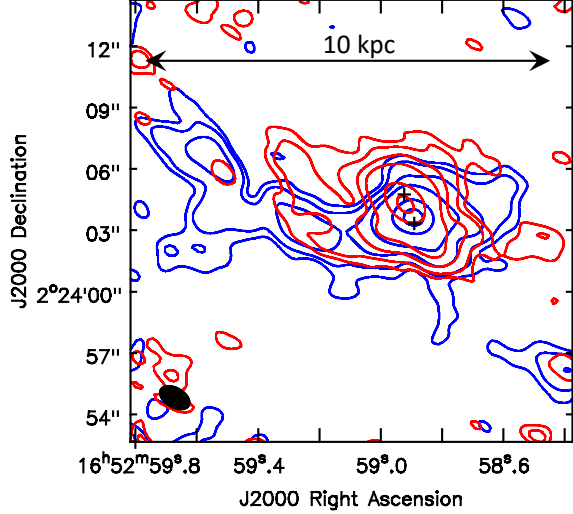


Figure 2. Comparison between the CO(2-1) blue and red wing emissions in NGC 6240. For visualisation purposes, only positive contours starting from 5σ are shown, with $1\sigma = 0.33 \text{ mJy beam}^{-1}$ for the blue wing (blue contours) and $1\sigma = 0.3 \text{ mJy beam}^{-1}$ for the red wing (red contours). The corresponding interferometric maps including negative contours are displayed in Appendix A (Figure 7).

Table 1. Results of the simultaneous fit to the total spectra*

	CO(1-0)	CO(2-1)	[CI](1-0)
Narrow component			
v^\dagger [km s ⁻¹]	-9.1 ± 1.0	-9.1 ± 1.0	-9.1 ± 1.0
σ_v [km s ⁻¹]	101.0 ± 1.0	101.0 ± 1.0	101.0 ± 1.0
S_{peak} [mJy]	211 ± 4	1058 ± 12	1360 ± 70
$\int S_\nu dv$ [Jy km s ⁻¹]	53.4 ± 1.0	268 ± 4	344 ± 18
L' [$10^9 \text{ K km s}^{-1} \text{ pc}^2$]	1.55 ± 0.03	1.94 ± 0.03	0.55 ± 0.03
Broad component			
v^\dagger [km s ⁻¹]	78.0 ± 1.2	78.0 ± 1.2	78.0 ± 1.2
σ_v [km s ⁻¹]	264.4 ± 1.0	264.4 ± 1.0	264.4 ± 1.0
S_{peak} [mJy]	301 ± 3	1458 ± 12	1040 ± 40
$\int S_\nu dv$ [Jy km s ⁻¹]	199 ± 2	966 ± 9	690 ± 30
L' [$10^9 \text{ K km s}^{-1} \text{ pc}^2$]	5.78 ± 0.06	7.01 ± 0.06	1.09 ± 0.05
Total line			
$\int S_\nu dv$ [Jy km s ⁻¹]	253 ± 2	1234 ± 10	1030 ± 30
L' [$10^9 \text{ K km s}^{-1} \text{ pc}^2$]	7.33 ± 0.07	8.96 ± 0.07	1.64 ± 0.05

* The errors quoted in this table are purely statistical and do not include the absolute flux calibration uncertainty.

† We employ the optical Doppler definition. The fit allows for a global velocity shift of CO(2-1) and [CI](1-0) with respect to CO(1-0) to take into account the different spectral binning. The best-fit returns:

$$v_{\text{CO}(2-1)} - v_{\text{CO}(1-0)} = 10.2 \pm 0.9 \text{ km s}^{-1} \text{ and}$$

$$v_{\text{[CI]}(1-0)} - v_{\text{CO}(1-0)} = -18 \pm 4 \text{ km s}^{-1}.$$

lar aperture reported in Fig 1(a), encompassing both the nucleus and the extended molecular outflow of NGC 6240. The analysis of these integrated spectra, described below, is aimed at deriving a source-averaged

α_{CO} for the quiescent and outflowing molecular ISM in NGC 6240. Such analysis is included here because it can be useful as a reference for unresolved observations, for example high redshift analogues of this merger. We stress however that the quality of our data, the proximity of the source, and its large spatial extent allow us to perform a much more detailed, spatially-resolved analysis. The latter will be presented in § 3.3 and delivers the most reliable α_{CO} values for the outflow and the quiescent gas.

The spectra in Fig. 4 were fitted simultaneously using two Gaussians to account for the narrow core and broad wings of the emission lines, by constraining the central velocity (v) and velocity dispersion (σ_v) of each Gaussian to be equal in the three transitions. Table 1 reports the best-fit results and the corresponding line luminosities calculated from the integrated fluxes following Solomon et al. (1997). The [CI](1-0) line luminosities listed in Table 1 are employed to measure the molecular gas mass (M_{mol} , including the contribution from Helium) associated to the narrow and broad line components. The expression for local thermodynamic equilibrium (LTE, i.e. uniform T_{ex}) and optically thin emission ($\tau_{\text{[CI]}(1-0)} \ll 1$), assuming a negligible background (CMB temperature, $T_{\text{CMB}} \ll T_{ex}$) and the Rayleigh-Jeans approximation ($h\nu_{\text{[CI]}(1-0)} \ll kT_{ex}$) is:

$$M_{mol}[M_\odot] = (4.31 \cdot 10^{-5}) \cdot X_{\text{CI}}^{-1} \cdot (1 + 3e^{-23.6/T_{ex}[\text{K}]} + 5e^{-62.5/T_{ex}[\text{K}]}) \cdot e^{23.6/T_{ex}[\text{K}]} \cdot L'_{\text{[CI]}(1-0)}[\text{K km s}^{-1} \text{ pc}^2], \quad (1)$$

where X_{CI} is the [CI]/H₂ abundance ratio and T_{ex} is the excitation temperature of the gas (see detailed explanations by Papadopoulos et al. (2004) and Mangum & Shirley (2015)). We adopt $T_{ex} = 30 \text{ K}$ and $X_{\text{CI}} = (3.0 \pm 1.5) \times 10^{-5}$, which are appropriate for (U)LIRGs (Weiß et al. 2003, 2005; Papadopoulos et al. 2004; Walter et al. 2011; Jiao et al. 2017). These assumptions will be further discussed in § 4.1.2.

By defining a [CI](1-0)-to-H₂ conversion factor ($\alpha_{\text{[CI]}}$) in analogy with the commonly employed α_{CO} factor (Bolatto et al. 2013), Eq 1 resolves into:

$$M_{mol}[M_\odot] \equiv \alpha_{\text{[CI]}} L'_{\text{[CI]}(1-0)}[\text{K km s}^{-1} \text{ pc}^2] \quad \text{with } \alpha_{\text{[CI]}} = 9.43 [M_\odot (\text{K km s}^{-1} \text{ pc}^2)^{-1}]. \quad (2)$$

Using the values in Table 1 and Eq 2, we obtain a total molecular gas mass of $M_{mol} = (1.5 \pm 0.8) \cdot 10^{10} M_\odot$, of which $(5 \pm 3) \cdot 10^9 M_\odot$ is in the narrow component, and $(10 \pm 5) \cdot 10^9 M_\odot$ in the broad wings. We then use these M_{mol} values to estimate α_{CO} :

$$\alpha_{\text{CO}} = M_{mol}[M_\odot] (L'_{\text{CO}(1-0)}[\text{K km s}^{-1} \text{ pc}^2])^{-1}. \quad (3)$$

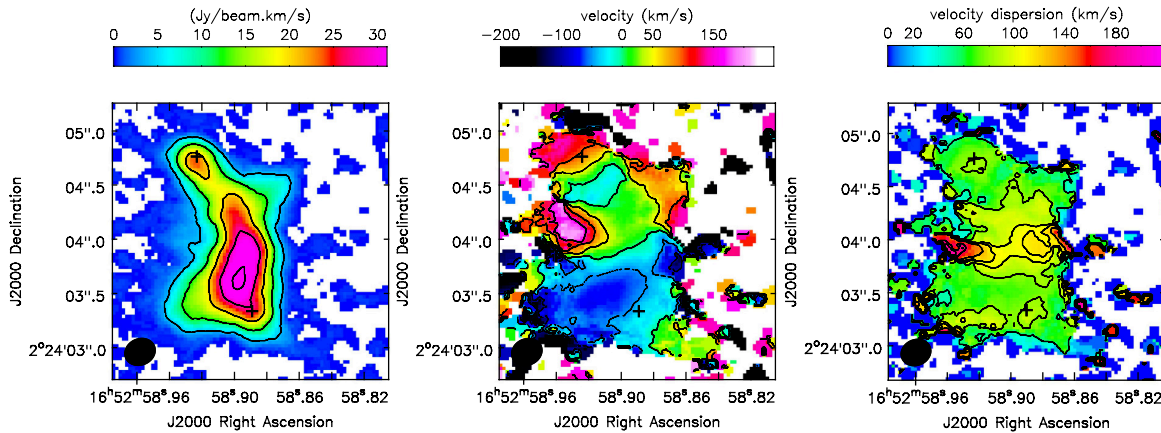


Figure 3. Intensity-weighted moment maps of the [CI](1-0) line emission in the merger nucleus. The maps were computed from the higher resolution ALMA+ACA merged data cube (see § 2) by using the task `immoments` and by selecting the spectral range $v \in (-200, 250)$ km s⁻¹. Contours correspond to: [-100, -50, 0, 50, 100, 150] km s⁻¹ (moment 1, *central panel*) and [50, 80, 100, 110, 130, 170, 180] km s⁻¹ (moment 2, *right panel*).

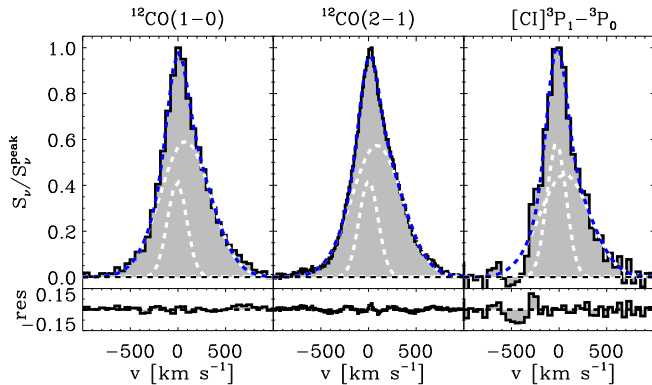


Figure 4. Total CO(1-0), CO(2-1), and [CI](1-0) spectra extracted from a $12'' \times 6''$ -size rectangular region centred at RA=16:52:58.900, Dec=02.24.03.950 and displayed in Fig. 1(a). The rms values per spectral channel are: 3.2 mJy ($\delta v = 53$ km s⁻¹), 17 mJy ($\delta v = 13$ km s⁻¹) and 78 mJy ($\delta v = 49$ km s⁻¹), respectively for CO(1-0), CO(2-1), and [CI](1-0). The spectra were simultaneously fitted using two Gaussian functions (white dashed curves) tied to have the same velocity and width in all three transitions. The best fit results are reported in Table 1. The source-averaged r_{21} and α_{CO} calculated from this fit are listed in Table 2.

The results are reported in the first three rows of Table 2 for the the total, narrow, and broad emissions in NGC 6240. The so-derived α_{CO} factors differ between the narrow and broad line components, being a factor of 1.8 ± 0.5 lower in the latter⁵. In the narrow component, the α_{CO} is significantly higher than the typical (U)LIRG value. As mentioned in § 1, higher α_{CO} values become possible in (U)LIRGs if a significant fraction of the mass

⁵ In estimating the error on this ratio we have ignored the systematic uncertainty on X_{CI} , assuming it affects both α_{CO} measurements in the same way.

is ‘hidden’ in dense and bound H₂ clouds. This is probably the case of NGC 6240, in which a large study using CO SLEDs from $J = 1 - 0$ up to $J = 13 - 12$ from the Herschel space observatory as well as multi- J HCN, CS, and HCO⁺ line data from ground-based observatories, finds $\alpha_{\text{CO}} \sim 2 - 4 M_{\odot} (\text{K km s}^{-1} \text{pc}^2)^{-1}$ (Papadopoulos et al. 2014), consistent with our estimates.

Table 2 lists also the CO(2-1)/CO(1-0) luminosity ratios, defined as

$$r_{21} \equiv L'_{\text{CO}(2-1)}/L'_{\text{CO}(1-0)}. \quad (4)$$

We find r_{21} consistently ~ 1.2 - hence higher than unity (at the 1.5σ level) - for both the narrow and broad Gaussian components. Since our total CO(1-0) and CO(2-1) fluxes are consistent with previous measurements (Papadopoulos et al. 2012b; Costagliola et al. 2011; Saito et al. 2018), we exclude that spatial filtering due to an incomplete uv coverage is significantly affecting the r_{21} values. As pointed out by Papadopoulos et al. (2012b), galaxy-averaged $r_{21} > 1$ values are not uncommon in (U)LIRGs and are indicative of extreme gas conditions. In this analysis of the integrated spectra we derived $r_{21} > 1$ in both the broad and narrow components. However, as we will show in § 3.3 and § 3.5, the spatially-resolved analysis will reveal that $r_{21} \gtrsim 1$ values are typical of the outflowing gas and in general of higher- σ_v components, while the ‘quiescent’ ISM has $r_{21} \sim 1$.

3.3. Spatially-resolved analysis: the average α_{CO} of the quiescent and outflowing gas

The previous analysis (§ 3.2) was based on the spectral fit shown in Fig. 4, where we decomposed the total molecular line emission into a narrow and a broad Gaussian. In first approximation, these two spectral compo-

Table 2. α_{CO} and r_{21} values*

	α_{CO} [$M_{\odot}(\text{K km s}^{-1} \text{pc}^2)^{-1}$]	r_{21}
Total [†]	2.1 ± 1.1	1.22 ± 0.14
Total [†] narrow comp	3.3 ± 1.8	1.25 ± 0.18
Total [†] broad comp	1.8 ± 0.9	1.21 ± 0.17
Mean [‡] global	2.5 ± 1.4	1.17 ± 0.19
Mean [‡] systemic comp	3.2 ± 1.8	1.0 ± 0.2
Mean [‡] outflow comp	2.1 ± 1.2	1.4 ± 0.3

* Quoted errors are dominated by systematic uncertainties (e.g. absolute flux calibration errors, error on X_{CI}).

[†] Calculated from the simultaneous fit to the total CO(1-0), CO(2-1), and [CI](1-0) spectra shown in Fig. 4, whose results are reported in Table 1 (details in § 3.2).

[‡] Mean values calculated from the simultaneous fit to the CO(1-0), CO(2-1), and [CI](1-0) spectra extracted from the grid of 13 boxes shown in Fig 1(a), as explained in § 3.3. The corresponding spectral fits are shown in Appendix B (Figs 8, 9, 10).

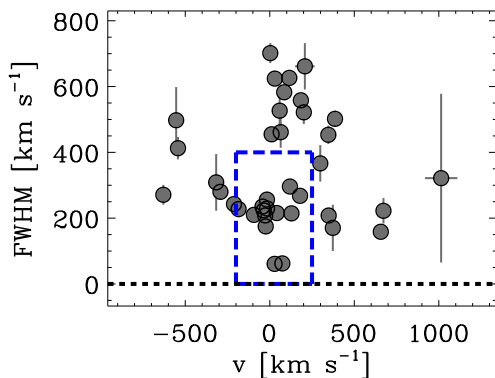


Figure 5. FWHM as a function of central velocity of all Gaussian components employed in the simultaneous fitting of the CO(1-0), CO(2-1), and [CI](1-0) box spectra. The blue dashed rectangle constrains the region of the parameter space that we ascribe to the ‘systemic’ components.

nents can be respectively identified with the quiescent and outflowing molecular gas reservoirs of NGC 6240. However, the superb S/N and spatial resolution of our data allow us to take this analysis one step further and refine the definition of quiescent and outflowing components. This is done by including the spatially-resolved information provided by the interferometric data, as described below.

We divide the central $12'' \times 6''$ region employed in the previous analysis into a grid of 13 squared boxes and use them as apertures to extract the corresponding CO(1-0), CO(2-1), and [CI](1-0) spectra. As shown in Fig. 1(a), the central nine boxes have a size of $2'' \times 2''$, while the external four boxes have a size of $3'' \times 3''$. The

box spectra are presented in Appendix B (Figures 8, 9, and 10).

For each box, the CO(1-0), CO(2-1), and [CI](1-0) spectra are fitted simultaneously with a combination of Gaussian functions tied to have the same line centres and widths for all three transitions. In the fitting procedure, we minimise the number of spectral components required to reproduce the line profiles, up to a maximum of four Gaussians per box. The Gaussian functions employed by the simultaneous fit span a wide range in FWHM and velocity, shown in Figure 5. The next step is to classify each of these components as ‘systemic’ or ‘outflow’. In many local (U)LIRGs molecular outflows can be traced through components whose kinematical and spatial features deviate from a rotating molecular structure (Cicone et al. 2014; García-Burillo et al. 2014). However, in this source we do not detect any clear velocity gradient that may indicate the presence of a rotating molecular gas disk (Figure 3). Therefore, we adopt a different method and identify as ‘quiescent’ the gas probed by the spectral narrow line components that are detected throughout the entire source extent (Figures 8, 9, and 10). Our simultaneous fit to the CO(1-0), CO(2-1), and [CI](1-0) spectra returns for these narrow components typical FWHM and central velocities in the ranges: $\text{FWHM} < 400 \text{ km s}^{-1}$ and $-200 < v[\text{km s}^{-1}] < 250$, consistent with what found by Feruglio et al. (2013a)⁶. Based on these results, we assume that all components with $-200 < v[\text{km s}^{-1}] < 250$ and $\text{FWHM} < 400 \text{ km s}^{-1}$ trace quiescent gas that is not involved in the outflow. These constraints correspond to the region of the FWHM- v parameter space delimited by the blue-dashed lines in Fig. 5. All components outside this rectangular area are classified as ‘outflow’. These assumptions are discussed in detail and validated in Appendix B, whereas more general considerations about our outflow identification method are reported in § 4.1.1.

Using the results of the simultaneous fit, we measure, for each box and for each of the CO(1-0), CO(2-1), and [CI](1-0) transitions, the velocity-integrated fluxes apportioned in the ‘systemic’ and ‘outflow’ components. These are computed by summing the fluxes from the respectively classified Gaussian functions fitted to the molecular line profiles. For example, in the case of the central box (labelled as ‘C1’ in Figs. 8, 9, and 10), the simultaneous fit employs three Gaussians: a narrow one classified as ‘systemic’, and two additional ones classified

⁶ Feruglio et al. (2013a) analysed the CO(1-0) spectra extracted from different positions within NGC 6240 and found maximum velocity shift and FWHM of the narrow Gaussians of $|v_{\text{sys}}^{\text{max}}| = 82 \pm 4 \text{ km s}^{-1}$ and $\text{FWHM}_{\text{sys}}^{\text{max}} = 380 \pm 150 \text{ km s}^{-1}$.

as ‘outflow’. The flux of the first Gaussian corresponds to the flux of the ‘systemic’ component for this box, whereas the total ‘outflow’ component flux is given by the sum of the fluxes of the other two Gaussians (the errors are added in quadrature).

The velocity-integrated fluxes (total, systemic, outflow) are then converted into line luminosities and, from these, the corresponding α_{CO} and r_{21} can be derived by following the same steps as in § 3.2 (Eq. 2-4). Table 2 (bottom three rows) lists the resulting mean values of α_{CO} and r_{21} obtained from the analysis of all 13 boxes. In computing the mean, we only include the components detected at a $S/N \geq 3$ in each of the transitions used to calculate α_{CO} or r_{21} , i.e. CO(1-0) and [CI](1-0) for the former, and CO(1-0) and CO(2-1) for the latter. The new α_{CO} values derived for the systemic and outflowing components, respectively equal to 3.2 ± 1.8 and 2.1 ± 1.2 , are perfectly consistent with the previous analysis based on the integrated spectra. Instead, this new analysis delivers different $\langle r_{21} \rangle$ values for the systemic (1.0 ± 0.2) and outflowing component (1.4 ± 0.3), although still consistent if considering the associated uncertainties (dominated by the flux calibration errors).

By using the CO(1-0) line data and summing the contribution from all boxes, including both the systemic and the outflowing components, we derive a total molecular gas mass of $M_{\text{mol}}^{\text{tot}} = (2.1 \pm 0.5) \times 10^{10} M_{\odot}$. To compute the M_{mol} within each box we adopt, when available, the ‘global’ α_{CO} factor estimated for that same box, otherwise we use the mean value of $\alpha_{\text{CO}} = 2.5 \pm 1.4^7$. Compared with previous works recovering the same amount of CO flux, our new $M_{\text{mol}}^{\text{tot}}$ estimate is higher than in Tacconi et al. (1999) and Feruglio et al. (2013b), but consistent with Papadopoulos et al. (2014).

3.4. Molecular outflow properties

In this section we use the results of the spatially-resolved spectral analysis presented in § 3.3 to constrain the mass (M_{out}), mass-loss rate (\dot{M}_{out}), kinetic power ($1/2\dot{M}_{\text{out}}v^2$), and momentum rate ($\dot{M}_{\text{out}}v$) of the molecular outflow. We first select the boxes in which an outflow component is detected in the CO(1-0) spectrum with $S/N \geq 3$. As described in § 3.3, the outflow component is defined as the sum of all Gaussian functions employed by the simultaneous fit that lie outside the rectangular region of the FWHM- v parameter space shown in Fig. 5. With this $S/N \geq 3$ constraint, 12 boxes

⁷ This was the case for the three boxes (labelled as ‘E1’, ‘W1’ and ‘W2’ in Figs. 8-10) without a $S/N \geq 3$ detection of [CI](1-0).

Table 3. Summary of source and outflow properties

Source properties:	
$L_{\text{TIR}(8-1000\mu\text{m})}$ [erg s ⁻¹]	$2.71 \times 10^{45(a)}$
L_{Bol} [erg s ⁻¹]	$3.11 \times 10^{45(b)}$
L_{AGN} [erg s ⁻¹]	$(1.1 \pm 0.4) \times 10^{45(c)}$
$\alpha_{\text{AGN}} \equiv L_{\text{AGN}}/L_{\text{Bol}}$	0.35 ± 0.13
SFR [M_{\odot} yr ⁻¹]	$46 \pm 9^{(d)}$
$M_{\text{mol}}^{\text{tot}}$ [M_{\odot}]	$(2.1 \pm 0.5) \times 10^{10(e)}$
Molecular outflow properties (estimated in § 3.4):	
r_{max} [kpc]	$2.4 \pm 0.3^{\ddagger}$
$\langle v_{\text{out}} \rangle$ [km s ⁻¹]	$250 \pm 50^{\ddagger}$
$\langle \sigma_{\text{out}} \rangle$ [km s ⁻¹]	$220 \pm 20^{\ddagger}$
$\langle \tau_{\text{dyn}} \rangle$ [Myr]	$6.5 \pm 1.8^{\ddagger}$
M_{out} [M_{\odot}]	$(1.2 \pm 0.3) \times 10^{10}$
\dot{M}_{out} [M_{\odot} yr ⁻¹]	2500 ± 1200
$v\dot{M}_{\text{out}}$ [g cm s ⁻²]	$(3.1 \pm 1.2) \times 10^{36}$
$1/2\dot{M}_{\text{out}}v^2$ [erg s ⁻¹]	$(3.6 \pm 1.6) \times 10^{43}$
$\eta \equiv \dot{M}_{\text{out}}/\text{SFR}$	50 ± 30
$(v\dot{M}_{\text{out}})/(L_{\text{AGN}}/c)$	80 ± 50
$(1/2\dot{M}_{\text{out}}v^2)/L_{\text{AGN}}$	0.033 ± 0.019
$\tau_{\text{dep}} \equiv M_{\text{mol}}^{\text{tot}}/\dot{M}_{\text{out}}$ [Myr]	8 ± 4

(^a) From the IRAS Revised Bright Galaxy Sample (Sanders et al. 2003); (^b) $L_{\text{Bol}} = 1.15 L_{\text{TIR}}$, following Veilleux et al. (2009); (^c) Total bolometric luminosity of the dual AGN system estimated from X-ray data by Puccetti et al. (2016); (^d) $\text{SFR} = (1 - \alpha_{\text{AGN}}) \times 10^{-10} L_{\text{TIR}}$, following Sturm et al. (2011). (^e) Total molecular gas mass in the $12'' \times 6''$ region encompassing the nucleus and the outflow, derived in § 3.4. [†] Maximum distance at which we detect [CI](1-0) in the outflow at a $S/N > 3$, hence the quoted r_{max} should be considered a lower limit constraint allowed by current data. [‡] Mean values obtained from the analysis of all boxes.

(that is, all except W1) are selected to have an outflow component in CO(1-0), and for each box ⁸ we measure:

(i) The average outflow velocity ($v_{\text{out},i}$), equal to the mean of the (moduli of the) central velocities of the individual Gaussians classified as ‘outflow’.

(ii) The molecular gas mass in outflow ($M_{\text{out},i}$), calculated by multiplying the $L'_{\text{CO}(1-0)}$ of each outflow component by an appropriate α_{CO} . In ten boxes the outflow component is detected with $S/N \geq 3$ also in the [CI](1-0) transition, hence for these boxes we can use their corresponding α_{CO} factor (see § 3.3). For the remaining two boxes (E1 and W2), we adopt the galaxy-averaged outflow α_{CO} of 2.1 ± 1.2 (Table 2).

(iii) The dynamical timescale of the outflow, defined as $\tau_{\text{dyn},i} = R_i/v_{\text{out},i}$, where R_i is the distance of the centre

⁸ All quantities relevant to the individual boxes are identified by an index $i = 1, 12$ (e.g. $v_{\text{out},i}$) in order to distinguish them from the corresponding galaxy-integrated quantities (e.g. v_{out}).

of the box from RA=16:52:58.900, Dec=02.24.03.950. This definition cannot be applied to the central box (C1) because the so-estimated R would be zero, hence boosting the mass-loss rate to infinite. Therefore, for box C1, we conservatively assume that most of the outflow emission comes from a radius of $1''$, hence we set $R = 0.5$ kpc. For all boxes we assume the uncertainty on R_i to be $0.6''$ (0.3 kpc), which is half a beam size.

(iv) The mass-loss rate $\dot{M}_{out,i}$, equal to $M_{out,i}/\tau_{dyn,i}$. All uncertainties are derived by error propagation.

The resulting total outflow mass and mass-loss rate, obtained by adding the contribution from all boxes, are respectively $M_{out} = (1.2 \pm 0.3) \times 10^{10} M_{\odot}$ and $dM_{out}/dt = 2500 \pm 1200 M_{\odot} yr^{-1}$. As discussed in Appendix B, the largest contribution to both \dot{M}_{out} and its uncertainty is given by the central box. Indeed, box C1 has at the same time the highest estimated M_{out} and the smallest - and most uncertain - R , because the outflow is launched from within this region, likely close to the mid-point between the two AGNs as suggested by Fig. 1(d,e).

Similar to the mass-loss rate, we calculate the total kinetic power and momentum rate of the outflow by summing the contribution from all boxes with a CO(1-0) outflow component, and we obtain respectively: $1/2\dot{M}_{out}v_{out}^2 \equiv \sum_i 1/2\dot{M}_{out,i}v_{out,i}^2 = (0.033 \pm 0.019) L_{AGN}$ and $v\dot{M}_{out} \equiv \sum_i v_i\dot{M}_{out,i} = (80 \pm 50) L_{AGN}/c$. If all the gas carried by the outflow escaped the system and the mass-loss continued at the current rate, the depletion time-scale of the molecular gas reservoir in NGC 6240 would be $\tau_{dep} = 8 \pm 4$ Myr. All the relevant numbers describing the properties of the source and of the molecular outflow are reported in Table 3 and will be discussed in § 4.3 in the context of feedback models.

Very stringent lower limits on the outflow energetics can be derived by assuming that its CO(1-0) emission is fully optically thin. For optically thin gas and $T_{ex} = 30$ K, the α_{CO} factor would be ~ 0.34 (Bolatto et al. 2013), and the outflow mass and mass-loss rate would be $M_{out} = (1.98 \pm 0.09) \times 10^9 M_{\odot}$ and $dM_{out}/dt = 430 \pm 160 M_{\odot} yr^{-1}$. We however stress that the assumption of fully optically thin CO(1-0) emission in the outflow is not supported by our data, which instead favour an α_{CO} factor for outflowing gas that is intermediate between the optically thin and the optically thick values (for solar metallicities).

3.5. Physical properties of quiescent and outflowing gas

Using the results of the spatially-resolved analysis presented in § 3.3, we now study how the α_{CO} and r_{21} parameters vary as a function of velocity disper-

sion (σ_v) and projected distance (d) from the nucleus of NGC 6240. The relevant plots are shown in Figure 6. To investigate possible statistical correlations, we conduct a Bayesian linear regression analysis of the relations in Fig. 6 following Kelly (2007)⁹.

The left panels of Fig. 6 do not indicate any statistically significant relation between α_{CO} and either σ_v or d . Instead, they show that the α_{CO} factor is systematically higher - although formally only at a significance of 1.2σ (Table 2) - in the quiescent gas than in the outflow, regardless of the velocity dispersion of the clouds, or of their position with respect to the merger nucleus. For the *non-outflowing* components, the α_{CO} factors are at least twice the so-called (U)LIRG value (Downes & Solomon 1998), and reach up to Galactic values. This result is consistent with the multi-transition analysis by Papadopoulos et al. (2014), and is likely due to the state of the dense gas phase that low- J CO lines alone cannot constrain, but which instead is accounted for when using [CI](1-0) as a molecular mass tracer. Nevertheless the *outflowing* H₂ gas has lower α_{CO} values than the quiescent ISM. This is indeed expected from the ISM physics behind α_{CO} for warm and strongly unbound gas states (Papadopoulos et al. 2012a), i.e. the type of gas that we expect to be embedded in outflows. In particular, in the case that molecular outflows are ubiquitous in (U)LIRGs as suggested by observations (Sturm et al. 2011; Veilleux et al. 2013; Spoon et al. 2013; Cicone et al. 2014), *the outflow may be the location of the diffuse and warm molecular gas phase that is not contained in self-gravitating cooler clouds - a sort of ‘intercloud’ medium advocated by some of the previous analyses based solely on low- J CO, ¹³CO line observations (Aalto et al. 1995; Downes & Solomon 1998)*. Furthermore, the flat trend between α_{CO} and d observed in Fig. 6 does not support the hypothesis that the lower α_{CO} values in (U)LIRGs are related to the collision of the progenitors’ disks, since in this case we would naively expect the lower α_{CO} clouds to be concentrated in the central regions of the merger. The α_{CO} values measured for the outflow components are however significantly higher than the optically thin value, suggesting that not all of the outflowing material is diffuse and warm, but there may still be a significant amount of dense gas. These results are further discussed and contextualised in § 4.2.

The right panels of Fig. 6 show a weak correlation between the r_{21} and σ_v (correlation coefficient, $\rho = 0.4 \pm 0.2$) and an anti-correlation with the distance, although only for the systemic/quiescent components ($\rho = -0.7 \pm$

⁹ We used the IDL routine `linmix_err.pro`

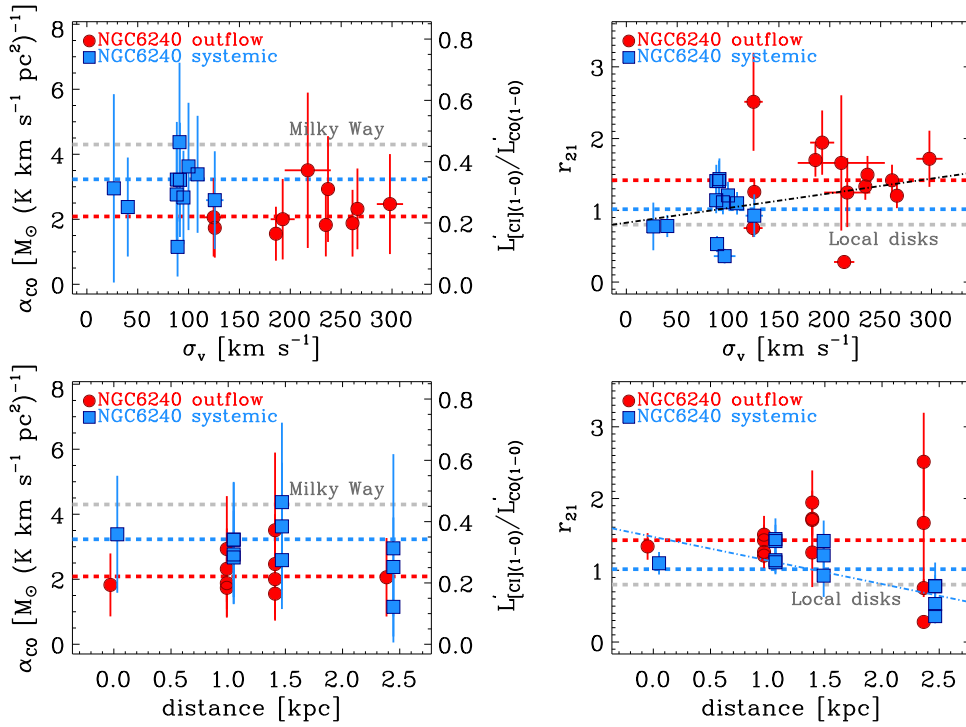


Figure 6. α_{CO} (left) and r_{21} (right) as a function of the average velocity dispersion (top) and of the distance from the nucleus (bottom) of the corresponding molecular line components. A detailed explanation on how α_{CO} and r_{21} were calculated can be found in § 3.3. The y axis on the right side of the α_{CO} plots shows the corresponding $[\text{CI}](1-0)/\text{CO}(1-0)$ line luminosity ratio. The horizontal blue and red dashed lines are the mean values reported in Table 2 for the systemic and outflow components, respectively. The grey lines indicate the Milky Way α_{CO} factor (Bolatto et al. 2013, left panels) and the average $r_{21} = 0.8$ measured in star forming galaxies (Leroy et al. 2009, right panels). The best-fits obtained from a Bayesian linear regression analysis following the method by Kelly (2007) are plotted using dot-dashed lines: black lines show the best fits to the total sample, whereas blue and red lines correspond to the fits performed separately on the systemic and outflowing components.

0.2). The corresponding best fit relations, of the form $r_{21} = \alpha + \beta x$, plotted in Fig. 6, have $(\alpha, \beta) = (0.8 \pm 0.2, 2.1 \pm 1.4 \times 10^{-3})$ for $x = \sigma_v$, and $(\alpha, \beta) = (1.5 \pm 0.2, -0.33 \pm 0.13)$ for $x = d$. The systemic ISM shows $0.8 \lesssim r_{21} \lesssim 1.4$, whereas the outflow is characterised by higher ratios, with most components in the range $1.2 \lesssim r_{21} \lesssim 2.5$, although we observe a large spread in r_{21} values at $d > 2$ kpc.

$\text{CO}(2-1)/\text{CO}(1-0)$ luminosity ratios of $r_{21} \sim 0.8 - 1.0$ are typically found in the molecular disks of normal spiral galaxies (Leroy et al. 2009) and are indicative of optically thick CO emission with $T_{\text{kin}} \sim 10 - 30$ K (under LTE assumptions). Nevertheless such low- J CO line ratios, in absence of additional transitions, are well-known to be highly degenerate tracers of the average gas physical conditions. Higher- J data of CO, molecules with larger dipole moment, and isotopologues can break such degeneracies. Such studies exist for NGC 6240 (Greve et al. 2009; Meijerink et al. 2013; Papadopoulos et al. 2014), and found extraordinary states for the molecular gas, with average densities typically above 10^4 cm^{-3} and temperatures $T_{\text{kin}} \sim 30 - 100$ K.

On the contrary, global $\text{CO}(2-1)/\text{CO}(1-0)$ ratios exceeding unity have a lower degree of degeneracy in terms of the extraordinary conditions that they imply for molecular gas, as they require warmer ($T_{\text{kin}} \gtrsim 100$ K) and/or strongly unbound states (Papadopoulos et al. 2012b). In NGC 6240, optical depth effects are most likely at the origin of the $r_{21} > 1$ values. More specifically, such ratios can result from highly non-virial motions (e.g. the large velocity gradients of the outflowing clouds), causing the CO lines to become partially transparent, as also supported by the tentative trend of increasing r_{21} with σ_v (Figure 6). This finding independently strengthens our explanation for the lower α_{CO} factors derived for the outflowing gas, which are intermediate between an optically thin and an optically thick value (for typical solar CO abundances).

4. DISCUSSION

4.1. Assumptions and caveats of our analysis

Our results build, on the one hand, on the identification of the outflow components, and on the other hand on the assumption that $\text{CO}(1-0)$ and $[\text{CI}](1-0)$ trace the same molecular gas, implying that M_{mol} can be mea-

sured from [CI](1-0). In this section we further comment on these steps and discuss their caveats and limitations.

4.1.1. *The outflow identification*

The outflow identification is a fundamental step of our analysis, and leads to one of the most surprising findings, i.e. that $60 \pm 20\%$ of the molecular ISM in NGC 6240 belongs to the outflow. This unprecedented result may hold the key to finally understanding the extreme ISM of this source, which makes it an outlier even compared to other (U)LIRGs, as acknowledged by several authors (Meijerink et al. 2013; Papadopoulos et al. 2014; Israel et al. 2015). For example, Meijerink et al. (2013) suggested that the CO line emission in NGC 6240 is dominated by gas settling down after shocks, which would be consistent with gas cooling out of an outflow. A massive outflow would also explain why the gaseous and stellar kinematics are decoupled (Engel et al. 2010; Tacconi et al. 1999).

In § 3.3 we have ascribed to the outflow all spectral line components with $\text{FWHM} > 400 \text{ km s}^{-1}$, $v < -200 \text{ km s}^{-1}$ or $v > +250 \text{ km s}^{-1}$ detected within the central $12'' \times 6''$ region investigated in this paper. However, the spatial information is also crucial for identifying outflowing gas, especially in a source undergoing a major merger, since the outflow signatures may be degenerate with gravity-driven dynamical effects. In the specific case of NGC 6240, as explained below and shown in detail in Appendix B, the high S/N and spatial resolution of our observations allow us to disentangle feedback-related effects from other mechanisms and reliably identify the outflow emission.

During a galaxy collision, high- v /high- σ_v gas can be concentrated in the nuclear region as a consequence of gravitational torques, which cause a fraction of the gas to lose angular momentum and flow toward the center. At the same time, gravitational torques and tidal forces can drive out part of the gas from the progenitors' disks and form large-scale filaments denominated 'tidal tails' and 'bridges'. However, in the case of NGC 6240, these gravity-induced mechanisms can hardly explain the kinematics and morphology of the ~ 10 kpc-scale, wide opening angle-emission shown in Figs. 1-3. In particular, the high- v /high- σ_v structures revealed by the [CI](1-0) moment maps, which are correlated with features observed on much larger scales (see § 3.1), cannot be due to nuclear inflows. In this case, we would indeed expect the σ_v of the gas to be enhanced toward the nucleus (or nuclei), rather than in offset positions that are several 100s of pc away from the nuclei or from the geometric center of the AGN pair (see for example the different signature of outflows and inflows

in the velocity dispersion maps shown by Davies et al. (2014)). The hourglass-shaped configuration visible in the [CI](1-0) velocity dispersion map is more suggestive of an outflow opening toward east and west, i.e. along the same directions of expansion of the high- v gas.

On larger scales, tidal tails or bridges produced in galaxy collisions may also affect the dynamical state of the ISM. However, the line-widths of the molecular emission from such filamentary structures are rather low ($\sim 50 - 100 \text{ km s}^{-1}$, Braine et al. 2001). Therefore, in order to reproduce the spatially- and kinematically-coherent structure shown in Figs. 1, and especially the spatial overlap across several kpc between the highly blue-shifted and red-shifted emissions (Figure 2), one would need to postulate a very specific geometry where several tidal tails overlap along the line of sight across more than 10 kpc.

Based on these considerations, and on the detailed discussion reported in Appendix B, we conclude that other mechanisms such as rotating disks or gravity-induced dynamical motions, possibly also coexisting in NGC 6240, are unlikely to significantly affect our outflow energetics estimates.

4.1.2. *Combining [CI](1-0) and CO(1-0) data to infer α_{CO} and M_{mol}*

The second key step of our analysis is to combine the [CI](1-0) and CO(1-0) line observations to derive molecular gas masses. As described in § 3.2-3.4, our strategy is to use the places where [CI](1-0) and CO(1-0) are both detected at a $\text{S/N} \geq 3$ to measure the corresponding α_{CO} . Molecular gas masses are then computed by using the CO(1-0) data. In particular, we select components where CO(1-0) is detected at a $\text{S/N} \geq 3$ and convert $L'_{\text{CO}(1-0)}$ into M_{mol} by employing either the corresponding [CI]-derived α_{CO} (possible only if [CI](1-0) is also detected with $\text{S/N} \geq 3$) or alternatively by using the mean α_{CO} value appropriate for that component (i.e. 'global', 'systemic', or 'outflow', Table 2).

The fundamental underlying assumption is that [CI](1-0) and CO(1-0) trace the same material. Earlier theoretical works envisioned neutral Carbon to be confined in the external (low extinction A_V) layers of molecular clouds, hence to probe a different volume compared to CO. However, as discussed by Papadopoulos et al. (2004), this theory was dismantled by observations finding a very good correlation between [CI] and CO as well as uniform [CI]/CO ratios across a wide range of Galactic environments, including regions shielded from FUV photons (e.g. Keene et al. 1985; Ojha et al. 2001; Tanaka et al. 2011). The few available observations of [CI] lines in local galaxies have further supported

the concurrence of CO and [CI] in different physical conditions (Israel et al. 2015; Krips et al. 2016).

The good mixing of CO and [CI] could be a consequence of turbulence and/or cosmic rays. Turbulent diffusion can merge any [CI]-rich H₂ phase (expected to prevail in low A_V regions) with the more internal CO-rich H₂ gas, hence uniforming the [CI]/CO abundance ratio throughout molecular clouds (Glover et al. 2015). Cosmic rays, by penetrating deep into molecular clouds and so destroying CO (but not H₂) over larger volumes compared to FUV photons, can also help enrich the internal regions of clouds with neutral Carbon (Bisbas et al. 2015, 2017). Both mechanisms are expected to be efficient in (U)LIRGs and in their molecular outflows. The latter are (by definition) highly turbulent environments. Furthermore, cosmic rays originating in the starburst nuclei can leak along such outflows hence influencing the chemistry of their embedded ISM (see discussion in Papadopoulos et al. (2018), and recent results by González-Alfonso et al. (2018)). For these reasons, we can assume that CO and [CI] trace the same molecular gas, for both the quiescent and outflowing components of NGC 6240.

Thanks to the simple three-level partition function of neutral Carbon, and to its lines being optically thin in most cases (including NGC 6240, Israel et al. (2015)), the main sources of uncertainties for [CI]-based mass estimates are X_{CI} and T_{ex} (Eq 1). Previous observations indicate very little variations in X_{CI} in the metal-enriched ISM of IR-luminous galaxies at different redshifts (Weiß et al. 2003, 2005; Danielson et al. 2011; Alaghband-Zadeh et al. 2013), including the extended ($r > 10$ kpc) circum-galactic medium of the Spiderweb galaxy (Emonts et al. 2018). In our calculations we assumed $X_{\text{CI}} = (3.0 \pm 1.5) \times 10^{-5}$ to take into account a systematic uncertainty associated with the [CI]/H₂ abundance ratio. Because of the particular LTE partition function of neutral Carbon, [CI]-derived masses depend little on T_{ex} for $T_{\text{ex}} \gtrsim 15$ K. We set $T_{\text{ex}} = 30$ K, which is consistent with the value that can be estimated from the global [CI]2-1/1-0 brightness temperature ratio measured in NGC 6240 (Papadopoulos et al. 2014).

Therefore, our assumptions regarding the conversion between [CI](1-0) line data and M_{mol} are well justified by previous results. However, we caution that a giant galactic-scale outflow such as the one hosted by NGC 6240 constitutes an unprecedented environment for molecular gas clouds, and there is no comparable laboratory in our Galaxy that can be used as a reliable reference. The study of the physical conditions of such outflows has only just started, and this is the first time that the [CI](1-0) line emission from high-velocity

gas components extending by several kpc has been imaged at high spatial resolution. Further investigation is needed, and our work constitutes just a starting point.

4.2. The role of outflows in the global α_{CO} factor

The average α_{CO} factors that we measure for the quiescent and outflowing components of the ISM in NGC 6240 (Table 2) are both higher than the classic (U)LIRG α_{CO} . How can we reconcile this result with previous works advocating for significantly lower α_{CO} values in (U)LIRGs? In the case of NGC 6240, our analysis has highlighted several effects that may have plagued previous α_{CO} estimates:

1. The widespread presence of outflowing gas implies that, at any location within this merger, the molecular line emission includes a significant contribution from the outflow, with its overall lower α_{CO} and higher r_{21} . As a result, an analysis of the global ISM conditions (especially if based only on low- J CO lines, see also point 3 below) would get contaminated by the warm unbound H₂ envelopes in the outflow, and their larger $L'_{\text{CO}}/M_{\text{H}_2}$ ratios would drive down the global α_{CO} estimate (Yao et al. 2003; Papadopoulos et al. 2012a).
2. The outflow dominates the velocity field of the H₂ gas throughout the entire source, including the central region (Figure 3). The apparent nuclear north-south velocity gradient identified in previous CO line data (Tacconi et al. 1999; Bryant & Scoville 1999) is actually not compatible with ordered rotation once observed at higher spatial resolution, but it shows several features distinctive of the outflow. Therefore, the assumption that the molecular gas in this area is dominated by ordered motions is broken, making any dynamical mass estimate unreliable (if the outflow is not properly taken into account).
3. Previous analyses based only on low- J CO lines have probably missed a substantial fraction of the denser gas phase that is instead accounted for when using the optically thin [CI](1-0) line as a gas mass tracer, or when probing the excitation of the ISM using high- J CO transitions and high density molecular gas tracers. Indeed, the α_{CO} value derived for the quiescent gas reservoir is consistent with a significant contribution from a dense gas state. Even in the outflow, the average α_{CO} is still significantly higher than the optically thin value, hence the presence of dense gas may not be negligible. A conspicuous dense gas phase has already been demonstrated in a few other galaxy-wide

molecular outflows (Aalto et al. 2012; Sakamoto et al. 2014; García-Burillo et al. 2014; Alatalo et al. 2015), and its presence would make more likely the formation of stars within these outflows (Maiolino et al. 2017).

4. The molecular gas emission in NGC 6240 is clearly very extended - both spectrally and spatially. As a result, at least some of the previous interferometric observations (especially ‘pre ALMA’) may have been severely affected by incomplete uv coverages filtering out the emission on larger scales, hence impacting on the measured line fluxes and sizes. Furthermore, as already noted by Tacconi et al. (1999), an insufficient spectral bandwidth may have hindered a correct baseline and/or continuum fitting and subtraction. The latter can be an issue for both single dish and interferometric observations, including observations with ALMA if only one spectral window is employed to sample the line.

Since molecular outflows are a common phenomenon in local (U)LIRGs (Sturm et al. 2011; Veilleux et al. 2013; Spoon et al. 2013; Cicone et al. 2014; Fluetsch et al. 2018), at least some of the above considerations may be generalised to their entire class. *Therefore, it is possible that the so-called (U)LIRG α_{CO} factor is an artefact resulting from modelling the molecular ISM of such sources containing massive H₂ outflows.*

4.3. An interplay of feedback mechanisms at work

The extreme spatial extent of its molecular outflow, makes NGC 6240 one of the few sources - all powerful quasars - hosting H₂ outflows with sizes of $\gtrsim 10$ kpc (Veilleux et al. (2017), see also the 30 kpc-size [CII] $\lambda 158\mu\text{m}$ outflow at $z = 6.4$ studied by Cicone et al. (2015)). In comparison, the H₂ gas entrained in the well-studied starburst-driven winds of M 82 and NGC 253 reaches at maximum scales of $\sim 1 - 2$ kpc (Walter et al. 2002, 2017). Furthermore, among all the large-scale molecular outflows discovered so far in quasar host galaxies, the outflow of NGC 6240 is the one that has been observed at the highest spatial resolution (~ 120 pc). Indeed, the ALMA [CI](1-0) line data allowed us to probe deep into the nuclear region of the merger, close to the launching point of the molecular wind, and surprisingly revealed that the outflow emission peaks between the two AGNs rather than on either of the two. This is apparently at odds with an AGN radiative-mode feedback scenario, in which the multi-phase outflow is expected to be generated close to the central engine (Costa et al. 2015).

Nevertheless, the role of the AGN(s) is certified by the extreme energetics of the molecular outflow, which has been constrained here with unprecedented accuracy. By comparing our M_{out} and $M_{\text{mol}}^{\text{tot}}$ estimates (Table 3), it appears that 60 ± 20 % of the molecular medium is involved in the outflow. The estimated mass-loss rate of $2500 \pm 1200 M_{\odot} \text{ yr}^{-1}$ corresponds to $\eta \equiv \dot{M}_{\text{out}}/\text{SFR} = 50 \pm 30$, whereas the lower limit on \dot{M}_{out} , calculated using the optically thin α_{CO} prescription, corresponds to $\eta \equiv \dot{M}_{\text{out}}/\text{SFR} = 9 \pm 4$. Such high mass loading factors are inconsistent with a purely star formation-driven wind. As a matter of fact, stellar feedback alone can hardly bear outflows with η much higher than unity. Cosmological hydrodynamical simulations incorporating realistic stellar feedback physics, by including mechanisms other than supernovae, can reach up to $\eta \sim 10$ (Hopkins et al. 2012). However, because η in these simulations anti-correlates with the mass of the galaxy, the highest η values are generally predicted for dwarf galaxies, whereas for galaxies with baryonic masses of several $10^{10} M_{\odot}$ such as NGC 6240, the η achievable by stellar feedback can be at maximum 2 – 3.

Based on its energetics, we can therefore rule out that the massive molecular outflow observed in NGC 6240 is the result of star formation alone. The outflow energetics can instead be fully accommodated within the predictions of AGN feedback models (Faucher-Giguère & Quataert 2012; Zubovas & King 2014; Costa et al. 2014). In addition, these models can explain the multi-wavelength properties of NGC 6240. At optical wavelengths, NGC 6240 is known to host a ionised wind (Heckman et al. 1990), with large-scale superbubbles expanding by tens of kpc towards north-west and south-east (Veilleux et al. 2003; Yoshida et al. 2016). The H α emission from the ionised wind shows a close spatial correspondence with the soft X-ray continuum, suggesting the presence of gas cooling out of a shocked medium (Nardini et al. 2013). Furthermore, Wang et al. (2014) detected a diffuse component in hard-X-ray continuum and FeXXV line emission, tracing $T \sim 7 \times 10^7$ K gas between the two AGNs (north-west of the southern nucleus, similar to the [CI](1-0) blue wing in Fig 1d), as well as in kpc-scale structures that are remarkably coincident with both the strong NIR H₂ emission (Max et al. 2005; van der Werf et al. 1993) and the H α filaments.

At radio wavelengths, Colbert et al. (1994) reported the detection of non-thermal continuum emission with a steep spectrum extending by several kpc in an arc-like structure west of the AGNs, later confirmed also by Baan et al. (2007), together with a possibly similar feature on the eastern side. This structure lacks a clear spatial correspondence with optical or NIR starlight (which

excludes a starburst origin) and its complex morphology suggests a connection with the $H\alpha$ outflow. Theoretically, the association between an AGN-driven wind and extended non-thermal radiation (due to relativistic electrons accelerated by the forward shock) has been predicted by Nims et al. (2015). Observationally, the rough alignment of the western arc-like structure discovered by Colbert et al. (1994) with the molecular outflow studied in this work would also support this hypothesis, although the current data do not allow us to probe the presence of H_2 outflowing gas at the exact position of the radio emission. The total radio power of this arc-like feature is comparable with that of extended radio structures previously observed in radio-quiet AGNs with prominent outflows (Morganti et al. 2016). Future facilities like the Cherenkov Telescope Array (CTA) may reveal the γ -ray counterpart of the non-thermal emission, as expected for an AGN outflow shock (Lamastra et al. 2017).

In summary, all these multi-wavelength observational evidences point to a radiative-mode AGN feedback mechanism (Faucher-Giguère & Quataert 2012; Nims et al. 2015). However, at the same time, it is difficult to reconcile a classic model with an H_2 outflow whose emission does not peak on either of the two AGNs. A complex interplay of stellar and AGN feedback must be at work in this source (see also Müller-Sánchez et al. 2018), and we cannot exclude the additional contribution from compact radio-jets (Gallimore & Beswick 2004), which may be accelerating part of the cold material (Mukherjee et al. 2016). Finally, positive feedback may also be at work in NGC 6240. There is indeed a striking correspondence between (i) the morphology of the approaching side of the outflow north-west of the southern AGN (Fig. 1d), (ii) a peak of dust extinction, and (iii) a stellar population with unusually large stellar σ_v and blue-shifted velocities (Engel et al. 2010). The latter, according to Engel et al. (2010), may have been formed recently as a result of crushing of molecular clouds, which could be related to the observed outflow event (Maiolino et al. 2017; Zubovas & King 2014) provided these stars are not older than a few Myr.

5. SUMMARY AND CONCLUSIONS

A powerful multiphase outflow shapes the distribution of gas in NGC 6240, and it is likely at the origin of many of the extraordinary features that for years have puzzled scientists studying this source. In this work we used new ALMA [CI](1-0) line observations, in combination with ALMA CO(2-1) and IRAM PdBI CO(1-0) line data, to study the morphology, energetics, and physical state of

the molecular component of the outflow. Our main findings are:

- The molecular outflow extends by more than 10 kpc along the east-west direction, and it is clearly detected in both its approaching (blue-shifted) and receding (red-shifted) sides. Its emission peaks between the two AGNs, rather than on either of the two. Furthermore, the outflow dominates the H_2 gas velocity field in the merger nucleus, as shown by the presence of a striking hourglass-shaped feature in the high-res ($\sim 0.24''$) [CI](1-0) line moment 2 map. This high- σ_v structure, aligned east-west, traces the launch base of the kpc-scale outflow. The outflow, with its large flux contribution to the molecular line emission in the nucleus, can explain both the high gas turbulence and the strong decoupling of stellar and gaseous kinematics evidenced in this source by previous works.
- We combined the [CI](1-0) and CO(1-0) line observations to derive the α_{CO} factor in the outflow, which is on average $\langle\alpha_{CO}\rangle = 2.1 \pm 1.2 M_{\odot}(\text{K km s}^{-1} \text{ pc}^2)^{-1}$. The information on the α_{CO} , in conjunction with a spatially-resolved spectral analysis of the molecular line emission, allowed us to constrain with unprecedented accuracy the energetics of the molecular outflow. We estimate that the outflow entrains $M_{out} = (1.2 \pm 0.3) \times 10^{10} M_{\odot}$, corresponding to 60 ± 20 % of the molecular reservoir of NGC 6240. The total mass-loss rate is $\dot{M}_{out} = 2500 \pm 1200 M_{\odot} \text{ yr}^{-1} = 50 \pm 30 \text{ SFR}$, which energetically rules out a solely star formation-driven wind.
- For the quiescent gas components, the α_{CO} factors are on average higher than in the outflow (irrespective of their distance from the nucleus), with a mean value of $\langle\alpha_{CO}\rangle = 3.2 \pm 1.8 M_{\odot}(\text{K km s}^{-1} \text{ pc}^2)^{-1}$, i.e. at least twice the so-called (U)LIRG value. This result is consistent with recent multi-transition ISM analyses and is likely due to a dense gas phase that cannot be constrained by using low-J CO lines alone, but which is instead accounted for when using [CI](1-0) as a molecular gas tracer.
- We observe a tentative trend of increasing r_{21} ratios with σ_v and measure $r_{21} > 1$ values in the outflow ($\langle r_{21} \rangle = 1.4 \pm 0.3$), while $r_{21} \simeq 1$ for quiescent gas. We explain the $r_{21} > 1$ ratios with optical

depth effects, whereby the highly non virial motions of the outflowing clouds cause the CO lines to become partially transparent.

- Based on the finding that lower α_{CO} and higher r_{21} values are typical of the outflowing clouds, we propose that molecular outflows are the location of the warm and strongly unbound phase - the ‘intercloud medium’ invoked by previous studies - that drives down the global α_{CO} in (U)LIRGs. However, we note that the [CI]-based α_{CO} factor derived for the outflow is higher than the optically thin value, suggesting that not all of the outflowing material is in such warm diffuse phase but that there may still be a significant amount of dense gas entrained.
- The outflow kinetic power and momentum rate, respectively equal to $(0.033 \pm 0.019) L_{\text{AGN}}$ and $(80 \pm 50) L_{\text{AGN}}/c$, could be fully accommodated within the predictions of AGN ‘blast-wave’ feedback models. However, the puzzling outflow morphology, with a launch region situated between the two AGNs, and a direction of expansion perpendicular to the axis connecting the two nuclei, challenges a classic AGN feedback scenario. A complex interplay of stellar and AGN feedback processes must be at work in NGC 6240.

This project has received funding from the European Union’s Horizon 2020 research and innovation pro-

gramme under the Marie Skłodowska-Curie grant agreement No 664931. The research leading to these results has received funding from the European Union’s Horizon 2020 research and innovation programme under grant agreement No 730562 [RadioNet]. R.M. acknowledges ERC Advanced Grant 695671 ‘QUENCH’ and support by the Science and Technology Facilities Council (STFC). E.T. acknowledges support from FONDECYT regular grant 1160999 and Basal-CATA PFB-06/2007. G.C.P. acknowledges support from the University of Florida. We thank the referee for his/her constructive report, which helped us improve the discussion of the results. This paper makes use of the following ALMA data: ADS/JAO.ALMA #2015.1.00717.S and #2015.1.00370.S. ALMA is a partnership of ESO (representing its member states), NSF (USA) and NINS (Japan), together with NRC (Canada), MOST and ASIAA (Taiwan), and KASI (Republic of Korea), in cooperation with the Republic of Chile. The Joint ALMA Observatory is operated by ESO, AUI/NRAO and NAOJ. This publication makes use of observations carried out with the IRAM Plateau de Bure Interferometer. IRAM is supported by INSU/CNRS (France), MPG (Germany) and IGN (Spain). C.C. thanks Sandra Burkutean for helping her with the combination of the ALMA and ACA B8 datacubes and Alvaro Hacar Gonzalez for suggesting to use the ACA B8 data as a source model in the cleaning of the ALMA B8 datacubes, which significantly improved the results.

Facilities: ALMA, IRAM PdBI

Software: CASA v4.6.0, GILDAS(Pety 2005)

REFERENCES

- Aalto, S., Booth, R. S., Black, J. H., & Johansson, L. E. B. 1995, *A&A*, 300, 369
- Aalto, S., Garcia-Burillo, S., Muller, S., et al. 2012, *A&A*, 537, A44
- . 2015, *A&A*, 574, A85
- Alaghband-Zadeh, S., Chapman, S. C., Swinbank, A. M., et al. 2013, *MNRAS*, 435, 1493
- Alatalo, K., Blitz, L., Young, L. M., et al. 2011, *ApJ*, 735, 88
- Alatalo, K., Lacy, M., Lanz, L., et al. 2015, *ApJ*, 798, 31
- Baan, W. A., Hagiwara, Y., & Hofner, P. 2007, *ApJ*, 661, 173
- Barcos-Muñoz, L., Aalto, S., Thompson, T. A., et al. 2018, *ApJL*, 853, L28
- Biernacki, P., & Teyssier, R. 2018, *MNRAS*, 475, 5688
- Bisbas, T. G., Papadopoulos, P. P., & Viti, S. 2015, *ApJ*, 803, 37
- Bisbas, T. G., van Dishoeck, E. F., Papadopoulos, P. P., et al. 2017, *ApJ*, 839, 90
- Bolatto, A. D., Wolfire, M., & Leroy, A. K. 2013, *ARA&A*, 51, 207
- Braine, J., Duc, P.-A., Lisenfeld, U., et al. 2001, *A&A*, 378, 51
- Brüggen, M., & Scannapieco, E. 2016, *ApJ*, 822, 31
- Bryant, P. M., & Scoville, N. Z. 1999, *AJ*, 117, 2632
- Carniani, S., Marconi, A., Maiolino, R., et al. 2015, *A&A*, 580, A102
- . 2017, *A&A*, 605, A105
- Cicone, C., Brusa, M., Ramos Almeida, C., et al. 2018, *Nature Astronomy*, 2, 176

- Cicone, C., Feruglio, C., Maiolino, R., et al. 2012, *A&A*, 543, A99
- Cicone, C., Maiolino, R., Sturm, E., et al. 2014, *A&A*, 562, A21
- Cicone, C., Maiolino, R., Gallerani, S., et al. 2015, *A&A*, 574, A14
- Colbert, E. J. M., Wilson, A. S., & Bland-Hawthorn, J. 1994, *ApJ*, 436, 89
- Combes, F., García-Burillo, S., Casasola, V., et al. 2013, *A&A*, 558, A124
- Costa, T., Rosdahl, J., Sijacki, D., & Haehnelt, M. G. 2018, *MNRAS*, 473, 4197
- Costa, T., Sijacki, D., & Haehnelt, M. G. 2014, *MNRAS*, 444, 2355
- . 2015, *MNRAS*, 448, L30
- Costagliola, F., Aalto, S., Rodriguez, M. I., et al. 2011, *A&A*, 528, A30
- Danielson, A. L. R., Swinbank, A. M., Smail, I., et al. 2011, *MNRAS*, 410, 1687
- Dasyra, K. M., & Combes, F. 2012, *A&A*, 541, L7
- Dasyra, K. M., Combes, F., Oosterloo, T., et al. 2016, *A&A*, 595, L7
- Davies, R. I., Maciejewski, W., Hicks, E. K. S., et al. 2014, *ApJ*, 792, 101
- Downes, D., & Solomon, P. M. 1998, *ApJ*, 507, 615
- Emonts, B. H. C., Lehnert, M. D., Dannerbauer, H., et al. 2018, *MNRAS*, 477, L60
- Engel, H., Davies, R. I., Genzel, R., et al. 2010, *A&A*, 524, A56
- Faucher-Giguère, C.-A., & Quataert, E. 2012, *MNRAS*, 425, 605
- Feruglio, C., Fiore, F., Piconcelli, E., et al. 2013a, *A&A*, 558, A87
- Feruglio, C., Maiolino, R., Piconcelli, E., et al. 2010, *A&A*, 518, L155
- Feruglio, C., Fiore, F., Maiolino, R., et al. 2013b, *A&A*, 549, A51
- Feruglio, C., Ferrara, A., Bischetti, M., et al. 2017, *A&A*, 608, A30
- Fiore, F., Feruglio, C., Shankar, F., et al. 2017, *A&A*, 601, A143
- Fischer, J., Sturm, E., González-Alfonso, E., et al. 2010, *A&A*, 518, L41
- Fluetsch, A., Maiolino, R., Carniani, S., et al. 2018, submitted to *MNRAS*, arXiv:1805.05352
- Gallimore, J. F., & Beswick, R. 2004, *AJ*, 127, 239
- García-Burillo, S., Combes, F., Usero, A., et al. 2014, *A&A*, 567, A125
- . 2015, *A&A*, 580, A35
- Gaspari, M., & Sądowski, A. 2017, *ApJ*, 837, 149
- Gerssen, J., van der Marel, R. P., Axon, D., et al. 2004, *AJ*, 127, 75
- Glover, S. C. O., Clark, P. C., Micic, M., & Molina, F. 2015, *MNRAS*, 448, 1607
- González-Alfonso, E., Fischer, J., Bruderer, S., et al. 2018, *ApJ*, 857, 66
- Gowardhan, A., Spoon, H., Riechers, D. A., et al. 2018, *ApJ*, 859, 35
- Greve, T. R., Papadopoulos, P. P., Gao, Y., & Radford, S. J. E. 2009, *ApJ*, 692, 1432
- Hacar, A., Tafalla, M., Forbrich, J., et al. 2018, *A&A*, 610, A77
- Hagiwara, Y., Baan, W. A., & Klöckner, H.-R. 2011, *AJ*, 142, 17
- Heckman, T. M., Armus, L., & Miley, G. K. 1990, *ApJS*, 74, 833
- Hopkins, P. F., Quataert, E., & Murray, N. 2012, *MNRAS*, 421, 3522
- Iono, D., Wilson, C. D., Takakuwa, S., et al. 2007, *ApJ*, 659, 283
- Ishibashi, W., & Fabian, A. C. 2015, *MNRAS*, 451, 93
- Israel, F. P., Rosenberg, M. J. F., & van der Werf, P. 2015, *A&A*, 578, A95
- Jiao, Q., Zhao, Y., Zhu, M., et al. 2017, *ApJL*, 840, L18
- Keene, J., Blake, G. A., Phillips, T. G., Huggins, P. J., & Beichman, C. A. 1985, *ApJ*, 299, 967
- Kelly, B. C. 2007, *ApJ*, 665, 1489
- King, A. R. 2010, *MNRAS*, 402, 1516
- Krips, M., Martín, S., Sakamoto, K., et al. 2016, *A&A*, 592, L3
- Lamastra, A., Menci, N., Fiore, F., et al. 2017, *A&A*, 607, A18
- Leroy, A. K., Walter, F., Bigiel, F., et al. 2009, *AJ*, 137, 4670
- Leroy, A. K., Walter, F., Martini, P., et al. 2015, *ApJ*, 814, 83
- Lindberg, J. E., Aalto, S., Muller, S., et al. 2016, *A&A*, 587, A15
- Maiolino, R., Russell, H. R., Fabian, A. C., et al. 2017, *Nature*, 544, 202
- Mangum, J. G., & Shirley, Y. L. 2015, *PASP*, 127, 266
- Max, C. E., Canalizo, G., Macintosh, B. A., et al. 2005, *ApJ*, 621, 738
- McMullin, J. P., Waters, B., Schiebel, D., Young, W., & Golap, K. 2007, in *Astronomical Society of the Pacific Conference Series*, Vol. 376, *Astronomical Data Analysis Software and Systems XVI*, ed. R. A. Shaw, F. Hill, & D. J. Bell, 127
- Meijerink, R., Kristensen, L. E., Weiß, A., et al. 2013, *ApJL*, 762, L16

- Morganti, R., Frieswijk, W., Oonk, R. J. B., Oosterloo, T., & Tadhunter, C. 2013, *A&A*, 552, L4
- Morganti, R., Veilleux, S., Oosterloo, T., Teng, S. H., & Rupke, D. 2016, *A&A*, 593, A30
- Mukherjee, D., Bicknell, G. V., Sutherland, R., & Wagner, A. 2016, *MNRAS*, 461, 967
- Müller-Sánchez, F., Nevin, R., Comerford, J. M., et al. 2018, *Nature*, 556, 345
- Nakai, N., Hayashi, M., Handa, T., et al. 1987, *PASJ*, 39, 685
- Nardini, E., Wang, J., Fabbiano, G., et al. 2013, *ApJ*, 765, 141
- Nims, J., Quataert, E., & Faucher-Giguère, C.-A. 2015, *MNRAS*, 447, 3612
- Ojha, R., Stark, A. A., Hsieh, H. H., et al. 2001, *ApJ*, 548, 253
- Oosterloo, T., Raymond Oonk, J. B., Morganti, R., et al. 2017, *A&A*, 608, A38
- Papadopoulos, P. P., Bisbas, T. G., & Zhang, Z. 2018, *MNRAS*, arXiv:1804.09654
- Papadopoulos, P. P., & Greve, T. R. 2004, *ApJL*, 615, L29
- Papadopoulos, P. P., Thi, W.-F., & Viti, S. 2004, *MNRAS*, 351, 147
- Papadopoulos, P. P., van der Werf, P., Xilouris, E., Isaak, K. G., & Gao, Y. 2012a, *ApJ*, 751, 10
- Papadopoulos, P. P., van der Werf, P. P., Xilouris, E. M., et al. 2012b, *MNRAS*, 426, 2601
- Papadopoulos, P. P., Zhang, Z.-Y., Xilouris, E. M., et al. 2014, *ApJ*, 788, 153
- Pety, J. 2005, in *SF2A-2005: Semaine de l’Astrophysique Française*, ed. F. Casoli, T. Contini, J. M. Hameury, & L. Pagani, 721
- Planck Collaboration, Ade, P. A. R., Aghanim, N., et al. 2016, *A&A*, 594, A13
- Puccetti, S., Comastri, A., Bauer, F. E., et al. 2016, *A&A*, 585, A157
- Richings, A. J., & Faucher-Giguère, C.-A. 2018, *MNRAS*, 474, 3673
- Saito, T., Iono, D., Ueda, J., et al. 2018, *MNRAS*, 475, L52
- Sakamoto, K., Aalto, S., Combes, F., Evans, A., & Peck, A. 2014, *ApJ*, 797, 90
- Sakamoto, K., Ho, P. T. P., & Peck, A. B. 2006, *ApJ*, 644, 862
- Sanders, D. B., Mazzarella, J. M., Kim, D.-C., Surace, J. A., & Soifer, B. T. 2003, *AJ*, 126, 1607
- Scoville, N., Sheth, K., Aussel, H., et al. 2016, *ApJ*, 820, 83
- Silk, J., & Rees, M. J. 1998, *A&A*, 331, L1
- Solomon, P. M., Downes, D., Radford, S. J. E., & Barrett, J. W. 1997, *ApJ*, 478, 144
- Spoon, H. W. W., Farrah, D., Leboutellier, V., et al. 2013, *ApJ*, 775, 127
- Sturm, E., González-Alfonso, E., Veilleux, S., et al. 2011, *ApJL*, 733, L16
- Tacconi, L. J., Genzel, R., Tecza, M., et al. 1999, *ApJ*, 524, 732
- Tanaka, K., Oka, T., Matsumura, S., Nagai, M., & Kamegai, K. 2011, *ApJL*, 743, L39
- Thompson, T. A., Fabian, A. C., Quataert, E., & Murray, N. 2015, *MNRAS*, 449, 147
- Thompson, T. A., Quataert, E., Zhang, D., & Weinberg, D. H. 2016, *MNRAS*, 455, 1830
- Turner, B. E. 1985, *ApJ*, 299, 312
- van der Werf, P. P., Genzel, R., Krabbe, A., et al. 1993, *ApJ*, 405, 522
- Veilleux, S., Bolatto, A., Tombesi, F., et al. 2017, *ApJ*, 843, 18
- Veilleux, S., Shopbell, P. L., Rupke, D. S., Bland-Hawthorn, J., & Cecil, G. 2003, *AJ*, 126, 2185
- Veilleux, S., Rupke, D. S. N., Kim, D.-C., et al. 2009, *ApJS*, 182, 628
- Veilleux, S., Meléndez, M., Sturm, E., et al. 2013, *ApJ*, 776, 27
- Walter, F., Weiß, A., Downes, D., Decarli, R., & Henkel, C. 2011, *ApJ*, 730, 18
- Walter, F., Weiss, A., & Scoville, N. 2002, *ApJL*, 580, L21
- Walter, F., Bolatto, A. D., Leroy, A. K., et al. 2017, *ApJ*, 835, 265
- Wang, J., Nardini, E., Fabbiano, G., et al. 2014, *ApJ*, 781, 55
- Weiß, A., Downes, D., Henkel, C., & Walter, F. 2005, *A&A*, 429, L25
- Weiß, A., Henkel, C., Downes, D., & Walter, F. 2003, *A&A*, 409, L41
- Wolfire, M. G., Hollenbach, D., & McKee, C. F. 2010, *ApJ*, 716, 1191
- Yao, L., Seaquist, E. R., Kuno, N., & Dunne, L. 2003, *ApJ*, 588, 771
- Yoshida, M., Yagi, M., Ohyama, Y., et al. 2016, *ApJ*, 820, 48
- Zhang, Z.-Y., Papadopoulos, P. P., Ivison, R. J., et al. 2016, *Royal Society Open Science*, 3, 160025
- Zschaechner, L. K., Walter, F., Bolatto, A., et al. 2016, *ApJ*, 832, 142
- Zubovas, K., & King, A. 2012, *ApJL*, 745, L34
- Zubovas, K., & King, A. R. 2014, *MNRAS*, 439, 400

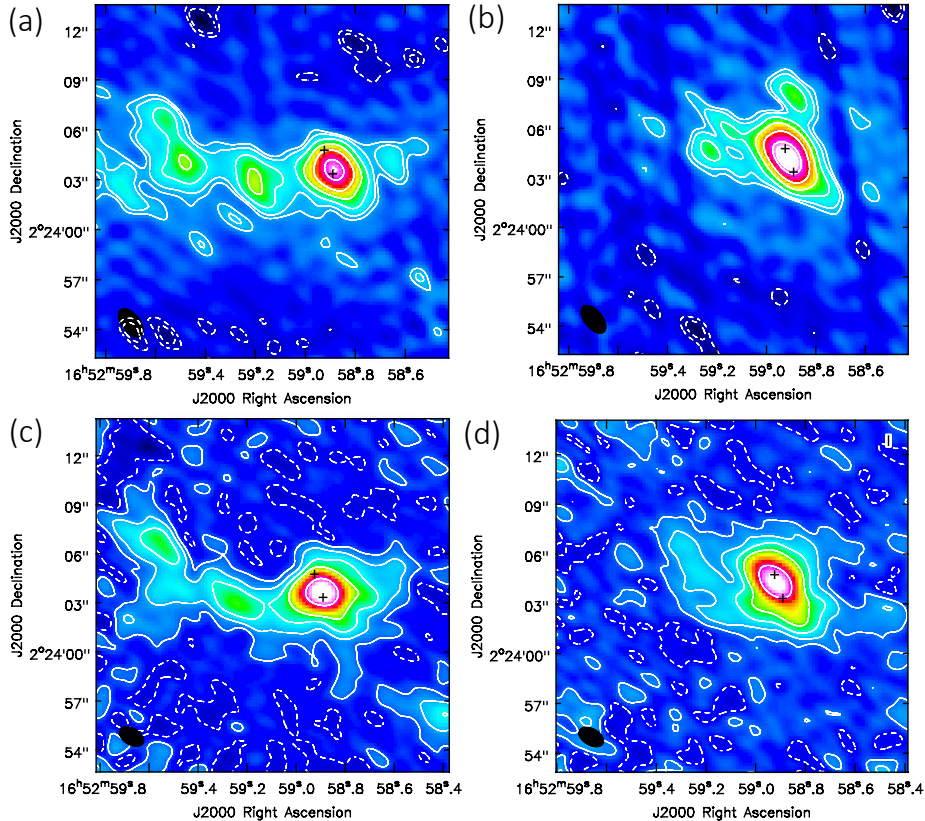


Figure 7. CO(1-0) (*top row*) and CO(2-1) (*bottom row*) interferometric maps of the outflow emission, integrated in the blue (*a, c*) and red (*b, d*) wings, by using the same velocity ranges as in Fig 1. The maps have matched spatial resolution ($\sim 1.2''$, details in § 2). Contours correspond to: $(-3\sigma, -2\sigma, 2\sigma, 3\sigma, 6\sigma, 12\sigma, 24\sigma, 48\sigma, 60\sigma)$ with $1\sigma = 0.33 \text{ mJy beam}^{-1}$ in panel (a) and $1\sigma = 0.39 \text{ mJy beam}^{-1}$ in panel (b); $(-3\sigma, 3\sigma, 10\sigma, 24\sigma, 48\sigma, 200\sigma, 350\sigma)$ with $1\sigma = 0.33 \text{ mJy beam}^{-1}$ in panel (c) and $1\sigma = 0.3 \text{ mJy beam}^{-1}$ in panel (d). Similar to Fig. 1, the black crosses indicate the VLBI positions of the AGNs from Hagiwara et al. (2011).

APPENDIX

A. ADDITIONAL CO(1-0) AND CO(2-1) OUTFLOW MAPS

Interferometric maps of the CO(1-0) and CO(2-1) high velocity emissions are shown in Fig. 7 separately for the blue (*left panels: a, c*) and red (*right panels: b, d*) line wings. To produce these maps, the CO(1-0) and CO(2-1) *uv* visibilities have been integrated within the same velocity ranges as in Fig. 1. Figure 7 demonstrates that the blue and red wings of the low-*J* CO lines in NGC 6240 are both spatially extended on scales of several kpc, with their most extended features aligned preferentially along the east-west direction. The positive contours of the CO(2-1) blue and red line wing emissions shown in Fig. 7(c,d) are overplotted in Figure 2 to allow a direct comparison of their extent and morphology.

B. BOX SPECTRA AND OUTFLOW IDENTIFICATION

The CO(1-0), CO(2-1), and [CI](1-0) box spectra extracted from the grid shown in panel (a) of Fig 1 are presented in Figures 8, 9, and 10. The results of the simultaneous fitting procedure described in § 3.3 are overplotted on the data. Each spectrum is labelled with the box ID: IDs C1-C9 correspond to the central $2'' \times 2''$ boxes, whereas E1-E2 and W1-W2 are respectively the eastern and western $3'' \times 3''$ boxes. The spectral components resulting from the simultaneous fit are classified as ‘outflow’ or ‘quiescent’ according to their velocity shift and dispersion, as described in § 3.3. In the following we examine - case by case - the results of such outflow identification procedure (see also § 4.1.1 for a more general discussion).

It is already evident from Fig.1(a,b,c) that the bulk of the molecular line emission at high projected velocities traces a very extended, non-collimated structure aligned east-west, with a large overlap between the blue and redshifted sides (Figure 2). As best seen in the high S/N CO(2-1) spectra in Fig. 9, the boxes E1, E2, W1, and W2, tracing gas at $d > 2$ kpc from the nucleus, exhibit broad spectral features - distinguishable from the narrow components - which in some cases (e.g. E1) dominate the total CO flux. Such broad wings are characterised by velocity shifts ($v \sim 300 - 600 \text{ km s}^{-1}$) and dispersions ($\sigma_v \sim 125 - 215 \text{ km s}^{-1}$) that are much higher than the narrow components detected in the same spectra ($v \sim 30 - 180 \text{ km s}^{-1}$, $\sigma_v \sim 30 - 100 \text{ km s}^{-1}$). As a result, we identify the high- v , high- σ_v spectral components at $d > 2$ kpc as due to an outflow.

Closer to the nucleus, the outflow identification becomes more challenging. However, once we have identified the broad components in E1, E2, W1, W2 as part of an outflow, then it is natural to ascribe similar broad components - spatially aligned along the east-west axis - to the same outflow. In particular, C4 and C8 (east and west of the nucleus), C2-C3 (north-west of the nucleus, along the same direction as the high- v structure in Fig. 1e) and C6-C7 (south-east of the nucleus, along another direction of outflow expansion as shown in Fig. 1d) also show a broad component extending up to $\sim 1000 \text{ km s}^{-1}$ on both the red- and blue-shifted sides. The outflow identification is more uncertain for boxes C5 and C9, where the wings are less prominent than in other regions, and the spatial alignment with the larger-scale outflow is not obvious. However, the contribution from these boxes to the total outflow mass and mass-loss rate is negligible. Indeed, without C5 and C9, we derive $M_{out} = 1.1 \times 10^{10} M_{\odot}$ and $dM_{out}/dt = 2350 M_{\odot} \text{ yr}^{-1}$, consistent with the values given in Table 3. Hence the uncertain outflow identification in boxes C5 and C9 does not affect our results.

We now discuss the central box C1, which alone contributes to: $M_{out}^{C1} = (4 \pm 2) \times 10^9 M_{\odot}$ and $dM_{out}^{C1}/dt = 1400 \pm 1100 M_{\odot} \text{ yr}^{-1}$. There are several arguments in support of a significant outflow contribution in this region: (i) the striking similarity between the C1 spectrum with that of the adjacent box C8; (ii) the notion that the outflow must originate from within this region, because it hosts two AGNs and most of the star formation activity; (iii) the [CI](1-0) emission at $|v| > 200 \text{ km s}^{-1}$ arising from within this region is spatially extended and follows the morphology of the larger-scale outflow (Figure 1(d,e)); (iv) in this region, the outflow dominates even the emission at low projected velocities, as shown by Fig. 3; (v) the α_{CO} and r_{21} values calculated for the outflow components identified in box C1 (data points at $d = 0$ kpc in the bottom panels of Fig. 6) are consistent with the values measured in the larger-scale outflow.

Therefore, based on the spectral and spatial properties of the molecular line emission that we have ascribed to the outflow, we conclude that alternative mechanisms such as rotating disks and tidal tails are unlikely to significantly affect our outflow energetics estimates.

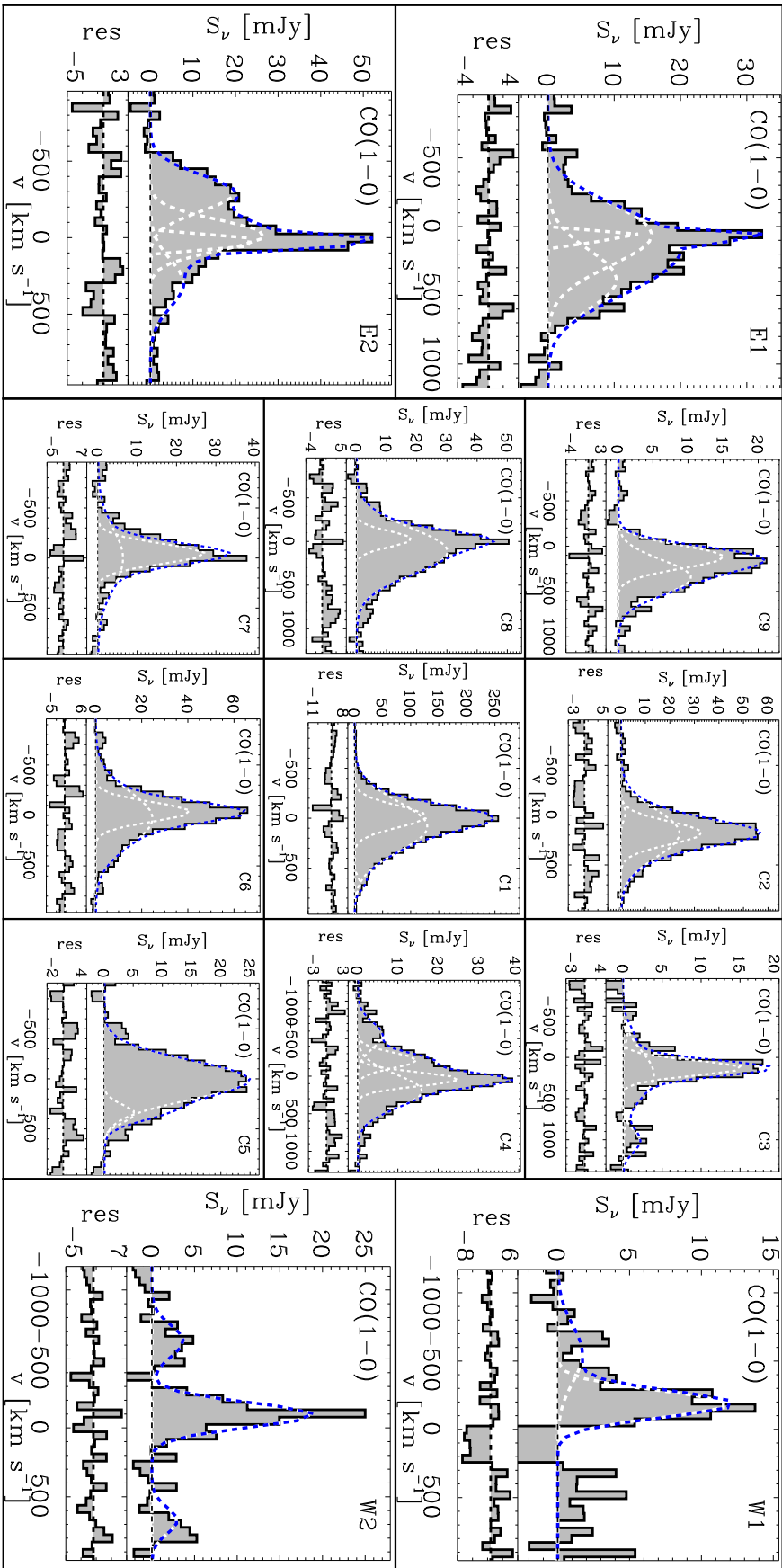


Figure 8. CO(1-0) spectra extracted from the grid of 13 boxes shown in panel (a) of Fig 1, with overplotted the results of the simultaneous fit procedure.

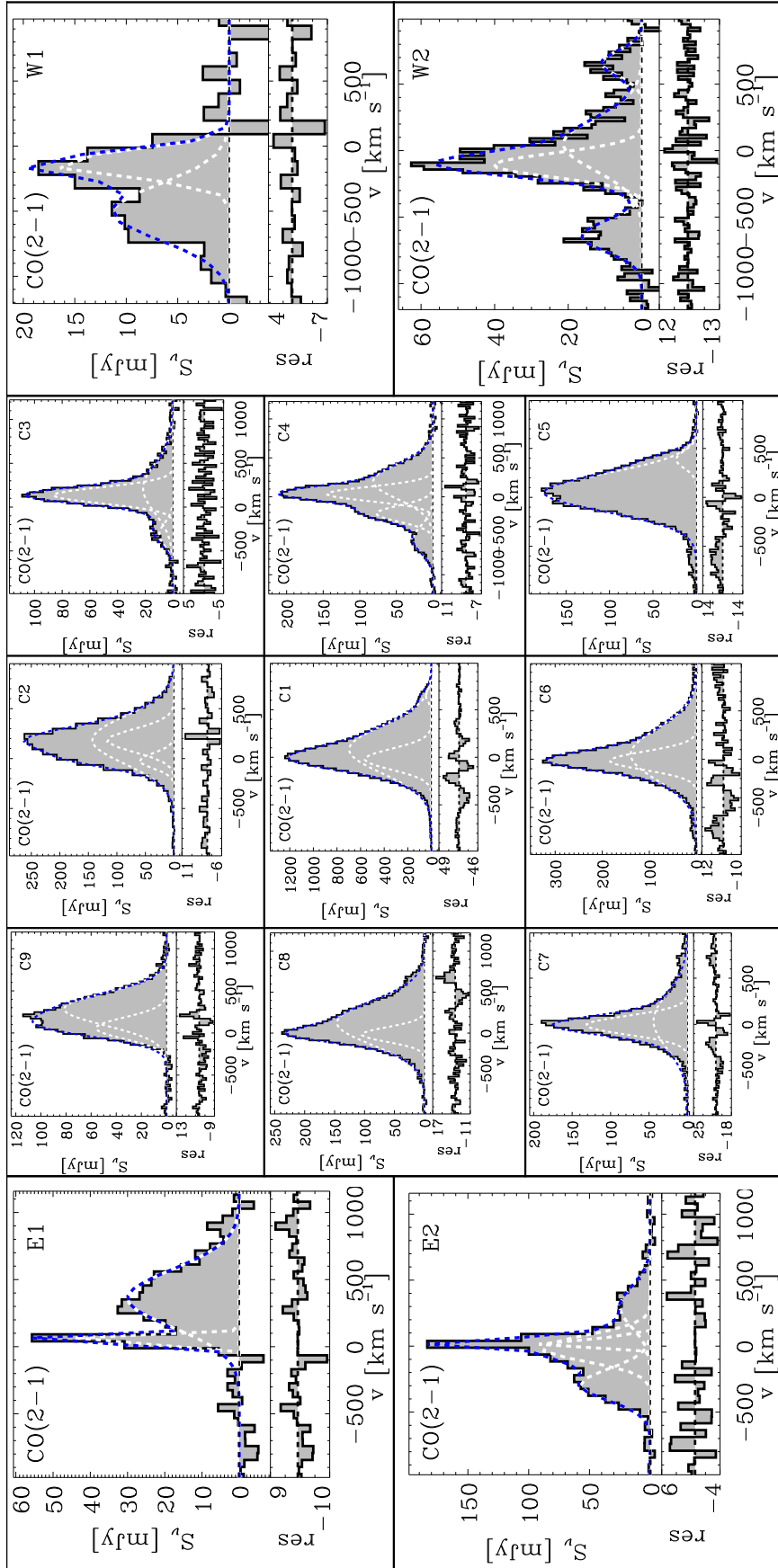


Figure 9. CO(2-1) spectra extracted from the grid of 13 boxes shown in panel (a) of Fig 1, with overplotted the results of the simultaneous fit procedure.

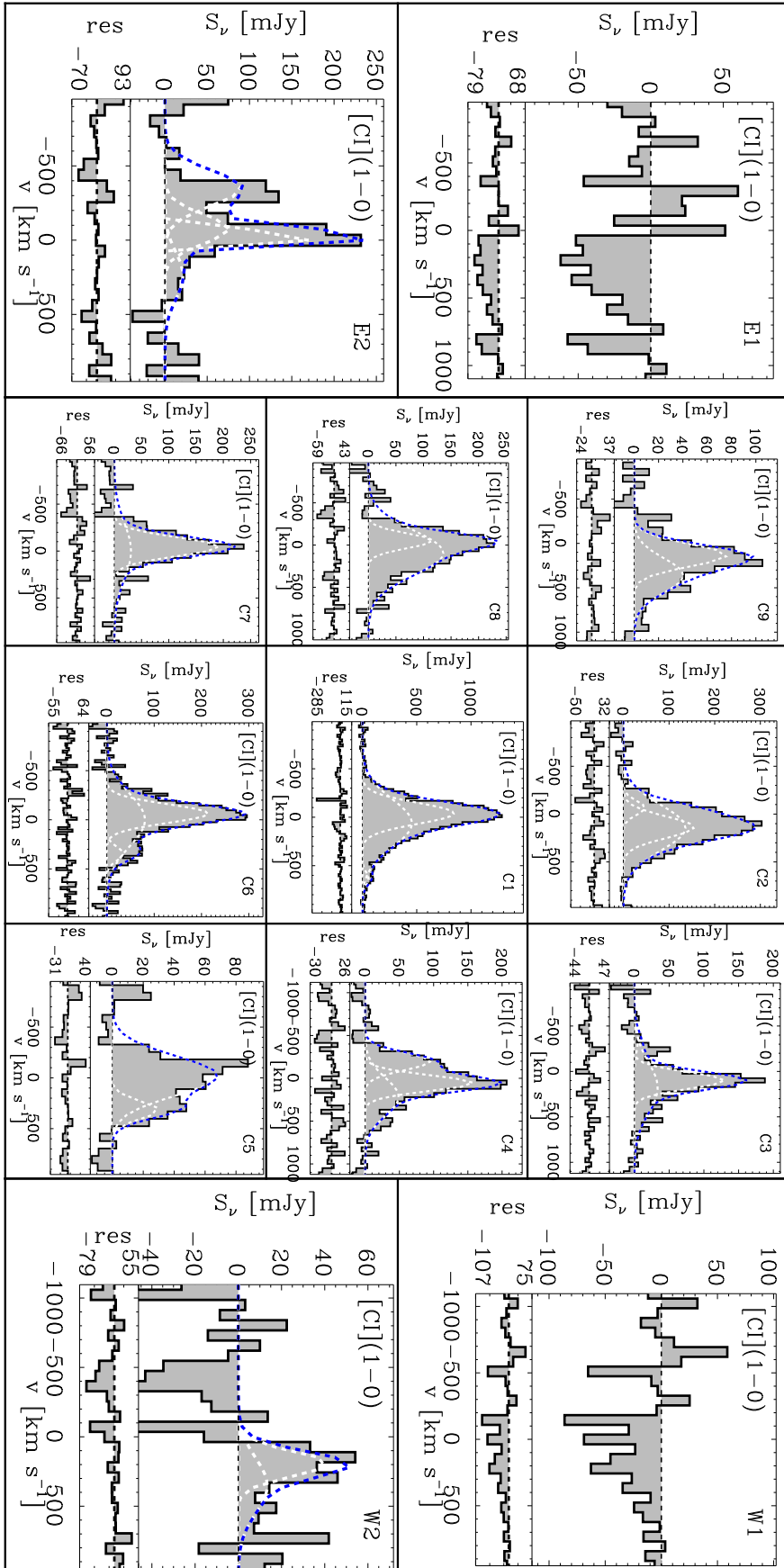


Figure 10. [C I](1-0) spectra extracted from the grid of 13 boxes shown in panel (a) of Fig. 1, with overlaid the results of the simultaneous fit procedure.